Available online at www.sciencedirect.com

SciVerse ScienceDirect

Procedia Engineering 00 (2012) 000–000

Procedia Engineering

www.elsevier.com/locate/procedia

5th BSME International Conference on Thermal Engineering

Tensile behavior of environment friendly jute epoxy laminated composite

Md. Rashnal Hossain* [a,b], Md. Aminul Islam [a], Aart Van Vuurea [b], Ignaas Verpoest [b]

[a]*Department of Materials & Metallurgical Engineering, Bangladesh University of Engineering and Technology, Dhaka-1000, Bangladesh*
[b]*Department of Metallurgy and Materials Engineering, Katholieke Universiteit Leuven, Kasteelpark Arenberg 44, 3001 Heverlee, Belgium*

Abstract

Jute fiber has gained interest in the composite field due to its superior specific properties compared to manmade synthetic fibers like glass, kevlar, asbestos, etc. In this study, jute composites were made with the vacuum assisted resin infiltration (VARI) techniques having jute fiber preform staking sequences (0/0/0/0), 0/+45°/-45°/0 and 0/90°/90°/0. For all cases, a total of 25% volume fraction of jute fiber was incorporated. The developed composites were characterized by tensile and three point bend tests and the experimental results thus obtained were compared with that of the theoretical values. After both mechanical tests, fracture surfaces were cut and observed under high resolution FEG SEM (field emission gun scanning electron microscopy). In the case of 0/0/0/0 and 0/+45°/-45°/0 laminate, longitudinal tensile strength has been found to be higher than that of the transverse direction. However, for 0/90°/90°/0 laminate, tensile strength in both directions have been found to be very close to each other. For all developed composites, experimental results revealed that the tensile properties of the developed composites are strongly dependent on the tensile strength of jute fiber and that the tensile properties of jute fiber are very much defect sensitive. Finally, initiative has also been taken to discuss the mechanical behaviors of the composites in terms of the fracture morphologies observed under the SEM.

© 2012 The authors, Published by Elsevier Ltd. Selection and/or peer-review under responsibility of the Bangladesh Society of Mechanical Engineers

Keywords: Jute, Laminate, Lumen, Resin penetration

---

1. Introduction

Jute as a natural fiber is eco-friendly, low cost, versatile in textile fields and has moderate mechanical properties, which replaced several synthetic fibers in development of many composite materials. However, the hydrophilic nature of the jute fiber affects the mechanical properties of the developed composites [1, 2]. Another important issue to note that the tensile strength of jute fiber is extremely defect and span sensitive. As a result, the stiffness values are usually corrected as per various failure strains following the proposed mathematical relationships [3, 4].

Usually, it is difficult to make unidirectional (UD) jute preform manually under dry condition [5]. Hackling under dry or wet condition introduces more defects on the fibrous preform. However, fiber matrix interface is better understood by UD composite [6, 7]. As a result, UD jute preform or roving preparation has become a valuable step and that, nowadays, it is gaining a great importance [8, 9].

Multidirectional isotropic behavior can be achieved by staking the UD ply in different angles, which yields composite with anisotropic physical and mechanical properties [10, 11]. Conventional composite fabrication procedures like

---

* Md. Rashnal Hossain. Tel.: +8801720433364;
E-mail address: hrashnal@gmail.com , hrashnal@yahoo.com

compression molding, hand–lay–up for jute like natural fiber, with moderately higher volume fraction (50%) of fiber reinforcement could produce composites of moderate to superior mechanical properties [12].

Synthetic fiber reinforced composite processing procedures are prepregging, resin transfer molding (RTM) and vacuum assisted resin infiltration (similar to RTM, but different in infiltration pressure) [13]. However, its versatility still attracted the intention of natural fiber composite researchers to utilize these techniques [14]. In this work, jute–thermoset continuous and angel ply laminated composites were made by vacuum assisted resin infiltration (VARI) technique and their mechanical properties (tensile and three point bend) were characterized.

1.1. Experimental

1.1.1 Materials and methods

In this research work retted, water washed and sun dried Bangla White Grade B (BWB) jute was collected from Bangladesh Jute Research Institute (BJRI) and single jute fiber tensile tests were carried out.

Four layer laminate preforms of size 400mmX400mm were made with jute fiber bunch and staking them in the following sequences (0/0/0/0), 0/+45°/-45°/0 and 0/90°/90°/0. Preforms were dried at 60°C overnight prior to composite fabrication.

As resin epoxy Epikote 828Lvel (Bisphenol A and Epichlorehydrin) and Diaminocyclohexane hardener were used. Then jute epoxy based composite was made employing standard VARI technique [13].

Tensile properties in longitudinal and transverse directions of the jute epoxy laminated composites were characterized as per ASTM D3039 standard. Three point bending as per ASTM D790 was also carried out to see the trend in strength and stiffness variation of the composites. Here 0˚ laminate direction is always taken as the principle loading direction.

After all mechanical tests, composite fracture surfaces were cut off and they were observed under a very high resolution FEG SEM of model PHILIPS XL30 FEG.

2. Results and discussion

2.1. BWB jute fiber properties

The tensile properties of used BWB jute and epoxy matrix are strength 844.72 ± 142.47 and 81.72 ± 13.16 MPa, stiffness 55.66 ± 2.11and 3.89 ± 0.53 GPa, and strain to failure 1.67% ± 0.31% and 2.23% ± 0.50% respectively [4]. But, as an anisotropic material, jute fiber has a large scatter in tensile properties depending on test specimen span length, test machine slippage and presence of inherent and surface of defects, which is graphically shown in Fig 1 a and b.

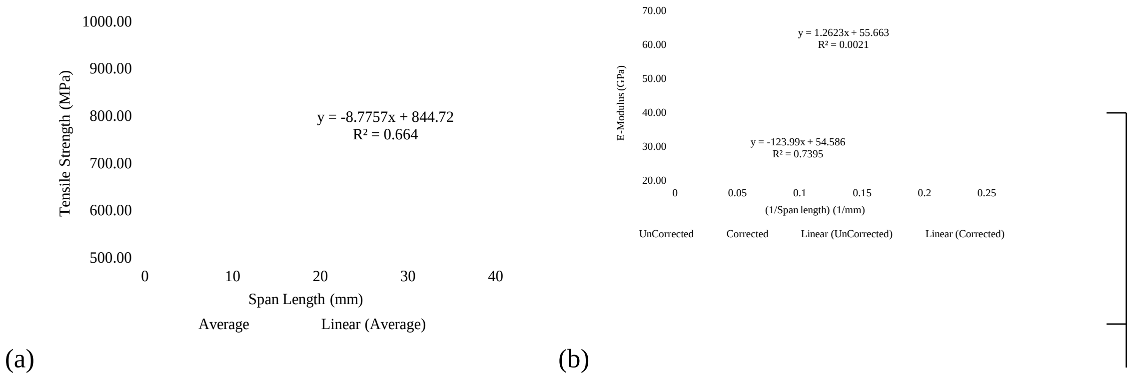

Fig. 1. Tensile strength and stiffness of BWB jute fiber in relation to span length; a) tensile strength curve and b) tensile stiffness curve.

Fig 1 represents the strength of BWB jute fiber as a function of test specimen lengths. The tensile strength of the jute fiber decreases with increase in the span length and scatter for each span is relatively higher for lower span length compared to that of the higher span length. The probability of finding a defect along the loading direction of fiber is very much unpredictable for low span. But for higher span the probability of finding a single or a number of defects are greater and so the tensile strength value is lower along with lower scatter band. On the other hand, stiffness/E-modulus/Young's modulus is independent of span length, defect of fiber and machine slippage [4]. Typical BWB jute fiber defects are shown in Fig 2.

This is since the load bearing part of the fiber is the cellulose micro fibril and the lower the micro fibril angle (jute micro fibril angle is less than 8°) the higher the mechanical properties [4]. Also cellulose micro fibril is the purest form of natural cellulose, which could be in crystalline and amorphous forms that contribute as the fiber stiffness enhancer similar to that of the fiber reinforcement in composite.

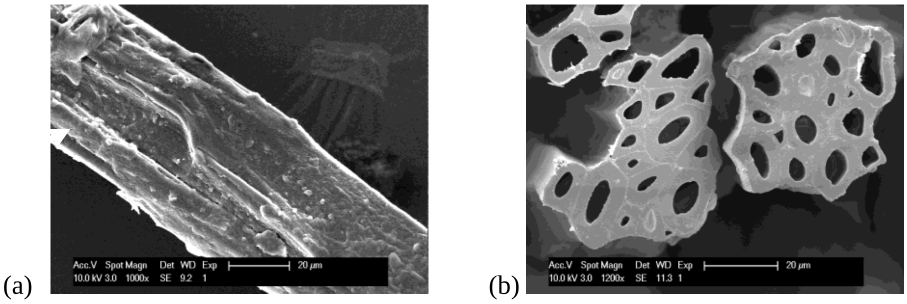

(a) (b)

Fig. 2. Typical defects of BWB jute fiber; a) lateral surface defect and b) cross-sectional defect.

3. Mechanical properties of composite laminates

Composite material is composed of two or more materials, where individual constituent material is not capable to provide required service properties. However, combination of the constituent materials provides the targeted service properties and reliability of the product. In this research work, jute reinforced epoxy based composites were developed to improve the service properties of epoxy. Concerning the experimental results, a common remark from Table 1 is that the longitudinal strength, stiffness and strain to failure in the principal (0°) loading direction have a decreasing trend with increasing laminate angle. Whereas, 0/+45/-45/0 laminate under three point load shows higher strength than unidirectional laminate due to fiber-fiber and fiber-matrix shearing in the +45/-45 angle. According to the rule of mixture, the 25 vol% reinforced BWB jute polymer composite should show yield strength 272.47MPa. But, practically, the developed composite showed the yield and three point bend strengths to be, respectively, 112.69 and 138.94 MPa (Table 2). These experimental results clearly revealed a significant loss in reinforcement efficiency, which has also been noticed by other [15]. The reason behind this efficiency loss is due to presence of defects in fibers of various concentrations and geometries.

Table 1. Longitudinal behaviour of laminate

Properties	Laminate Type	Strength MPa	SD	Strain To Failure	SD	Stiffness Gpa	SD
Tensile	0-0	112.69	18.31	0.82%	0.17%	14.59	2.28
	0-45	64.31	13.18	0.64%	0.15%	10.46	0.56
	0-90	42.54	6.42	0.43%	0.05%	11.13	1.47
3PBT	0-0	138.94	18.62	1.94%	0.70%	10.31	3.95
	0-45	149.71	20.19	1.99%	0.43%	9.88	2.13
	0-90	106.27	20.44	1.98%	0.45%	7.61	1.95

Table 2. Transverse behavior of laminates

Properties	Laminate Type	Strength MPa	SD	Strain To Failure	SD	Stiffness Gpa	SD
Tensile	0-0	11.06	3.30	0.35%	0.04%	3.25	0.62
	0-45	21.33	2.08	0.80%	0.38%	4.46	0.64
	0-90	39.10	10.85	0.53%	0.19%	8.97	0.74
3PBT	0-0	18.24	7.79	1.12%	0.30%	1.68	0.38
	0-45	49.44	8.01	3.67%	0.69%	3.34	0.67
	0-90	50.71	8.13	2.84%	0.15%	2.95	0.43

Transverse mechanical properties of the fabricated composites are shown in Table 2. The strength value in both tensile and 3 point bending showed increasing trend with increasing laminate angle. From Table 1 and 2, we notice that the 0-90 laminate posses similar types of strength and stiffness properties. The strain value of 0-45 laminate under 3 point bend load is distinctly higher and close to 4%. The reason behind this will be explained latter.

3.1. Fracture analysis of UD and 0 – 90 composite

The jute fibers surface conditions are not always similar and the probability of larger size defects in long span test specimen is also high. As a result, compatibility and adhesion between jute fiber and the matrix vary, which also contributes to lower tensile strength of the developed composites.

Tensile strength in the transverse direction is also lower than that of the theoretical values and significantly lower than that of the longitudinal direction. The probable reason could be mixed mode fiber-matrix interfaces. Along with this inhomogeneous fiber content, irregular bonding between matrix/fiber interfaces, voids, inherent defects of the jute fiber, etc. seriously degrade the tensile strength of the composite [15]. As a consequence of the combined degrading effects, the experimental strength of the composites in the transverse direction becomes significantly lower than that of the longitudinal direction. Ultimately, in any direction, the maximum fiber strength efficiency has not been achieved.

The higher values of tensile strengths in the longitudinal direction can be explained by fracture morphology as shown in Fig 3. In this case, at first, matrix was broken because of its relatively lower tensile strength followed by fiber matrix debonding and pullout. At last stage, jute fiber having relatively higher tensile strength was broken. The sequence of events could be; a) loading, b) matrix cracking and crazing, c) fiber/matrix interface or inter-phase debonding, d) start of fiber failure, e) further debonding and pullout of fiber from matrix, and f) final fiber failure followed by composite failure. As the jute fiber has a high tensile strength, so the composite showed higher tensile strength in the longitudinal direction.

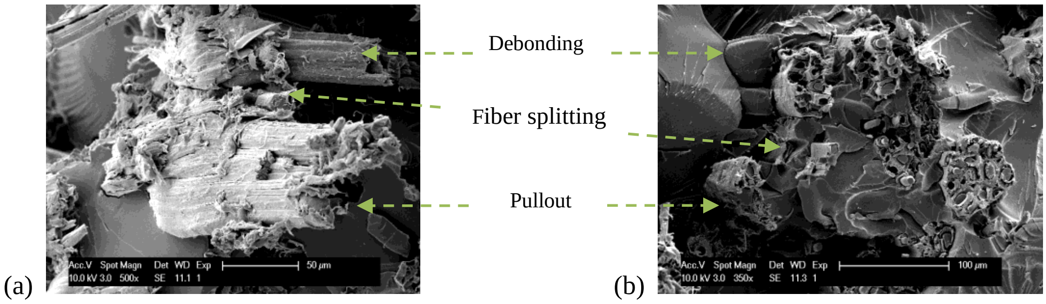

Fig. 3. Composite failure modes under longitudinal loading; a) tensile fracture and b) 3 point bending fracture.

In the case of transverse direction, tensile failure of 0/0 laminate jute fiber composites fiber slicing and debonding at fiber/matrix interfaces have been found to be dominating mode of fracture, Fig 4. Here, most of the cross sectional area is covered by the weak fiber/matrix interface and/or bunch of jute fiber. As a result, for 0/0 laminate of jute fiber composites a drastic decrease in tensile strength was observed.

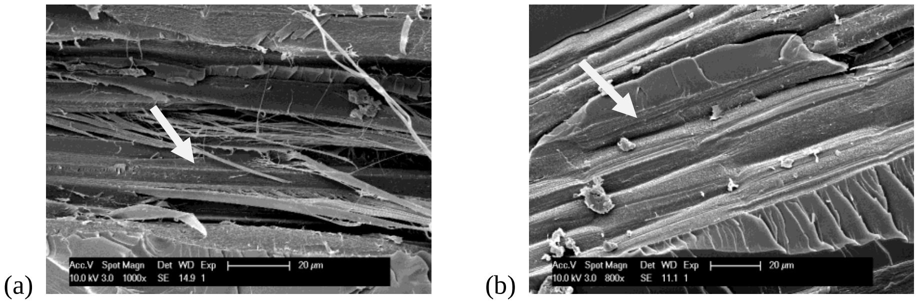

Fig. 4. Fiber and matrix failure under transverse tensile load; a) fiber slicing and b) fiber matrix debonding (3 point bending).

3.2. Fracture analysis of 0/+45/-45/0 composite

The lower strength of 0/+45/-45/0 laminate in the principle loading direction is attributed to matrix dominated shear force, which inherently dependent on the lower fiber volume fraction (25%) of reinforcement. Along with this, the higher transverse strength in this direction is due to the higher shear-force acting between ±45° laminate layers.

Fig 5 indicates the typical fracture surface of 0/+45/-45/0 composite under longitudinal load. Failure is characterized by matrix fiber matrix shearing, matrix and fiber shearing. Some fiber pullout in ±45° direction is also observed. Since, there is fiber matrix shearing, so fiber debris is also observed during 3 point bending. Large matrix crack owing to shearing effect is a characteristic failure criteria of jute epoxy 0/+45/-45/0 composite under the three point bend load as indicated rectangle in Fig 5b.

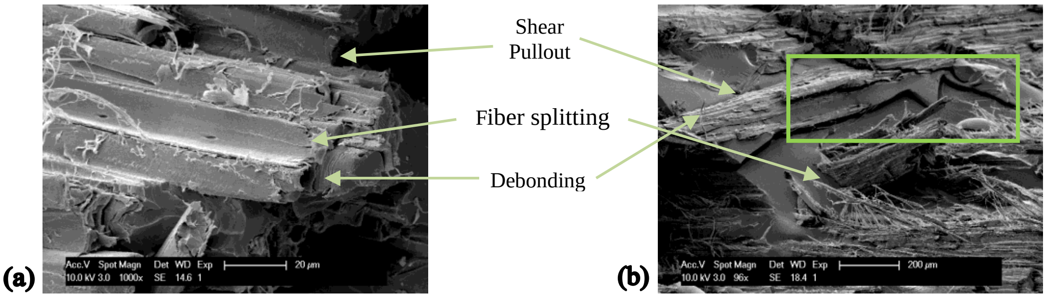

Fig. 5. Fiber and matrix failure under transverse tensile load; a) fiber slicing and b) debonding.

Another characteristic failure feature of 0-45 laminate under transverse loading is fiber matrix interface failure indicated by shear-lip type wavy fracture surface; Fig 6.

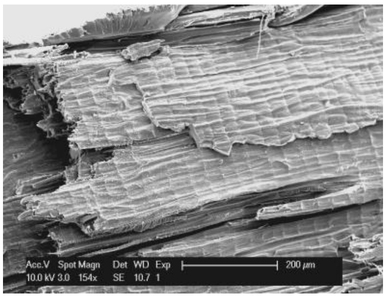

Fig. 6. Fracture surface of 0/+45/-45/0 composite laminate under transverse load showing fracture of share-lip type wavy nature.

Matrix failure in spherulitic fashion indicates the presence of compressive force around fiber (marked by arrow) as shown in Fig 7a. This compressive zone is more brittle than the surrounding matrix and shows the tendency of matrix cracking under longitudinal load in principal loading direction. This presence of compressive force is confirmed by crazing zone (marked by arrow) around fiber under transverse loading condition, which is shown in Fig 7b. In this loading condition brittle fiber failure (marked by arrow) is also observed as indicated by arrow in Fig 7c.

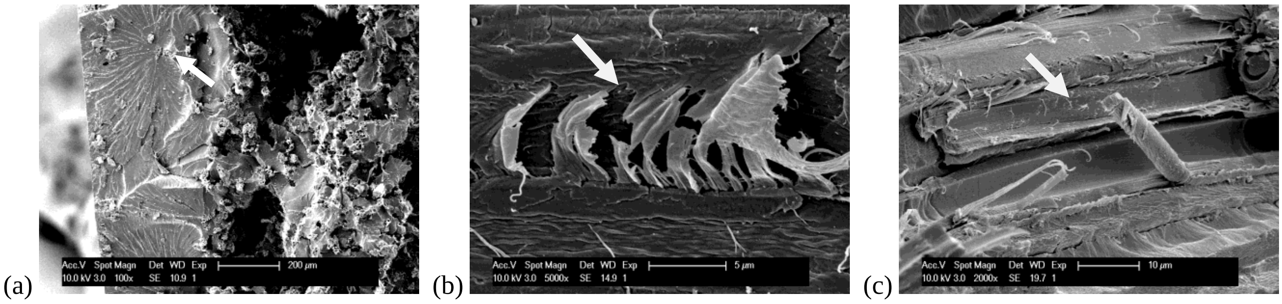

Fig. 8. Crazing of jute epoxy composite under transverse tensile loading; a) spherulitic failure, b) crazing and c) fiber failure.

4. Conclusion

In this research work, vacuum assisted resin infiltration (VARI) techniques with preform staking sequences (0/0/0/0), 0/+45°/-45°/0 and 0/90°/90°/0 were used to fabricate the composites. From this research work, the following conclusions are made.

- In longitudinal direction, the tensile strength and stiffness of 0-0 laminate composites have been found to be higher compared to that of 0-45 or 0-90 laminate composites. In the same direction, however, the trends for bending strength test results were opposite. The higher values of tensile strengths in the longitudinal direction was due to higher degree of fiber pull out in this direction, which caused a relatively higher level of fracture surface.

- In transverse direction, both the tensile and bending strengths 0-0 laminate composites have been found to be lower compared to that of 0-45 or 0-90 laminate composites. In the case of transverse direction of 0/0/0/0 (UD) composites the reinforced jute fiber experienced drastic slicing and fibrillation. This behavior of jute fiber is believed to be the main reason for the poor transverse mechanical properties of the developed composite. Compared to transverse three point bending of 0/0/0/0 (UD) composite 0/+45/-45/0 composite showed higher strength. This relatively higher strength of 0/+45/-45/0 composite is due to the shear lip type fracture surface.

Acknowledgements

The authors sincerely acknowledge the support of Department of Metallurgy and Materials Engineering, Katholieke Universiteit Leuven, Kasteelpark Arenberg 44 bus 2450, 3001 Heverlee, Belgium. They also acknowledge the cooperation of Materials and Metallurgical Engineering Department, BUET, Dhaka-1000.

References

[1] Vazqueza A., and Plackett D., 2004. Natural polymer sources, Woodhead Publishing Ltd & C.R.C. Press L.L.C., U.K.
[2] Liu X. Y., Dai G. C., 2007. Surface modification and micromechanical properties of jute fiber mat reinforced polypropylene composites, eXPRESS Polymer Letters 1(5), p. 299.
[3] Yu J.Y., Xia Z.P., Cheng L.D., Liu L.F., Wang W.M., 2009. Study on the breaking strength of jute fibres using modified Weibull distribution, Composites: Part A 40, p. 54.
[4] Defoirdt N., Biswas S., Vriese De L.e, Ngoc Tran L. Q., Van Acker J., Ahsan Q., Gorbatikh L., Van Vuure A., Verpoest I., 2010. Assessment of the tensile properties of coir, bamboo and jute fibre, Composites: Part A 41, p. 588.
[5] Mishra, S. P. 2005. A Text Book of Fiber Science and Technology, New Age International (P) Limited, India.

[6] Eichhorn S. J., Baillie C. A., Zafeiropoulos N., Mwaikambo L. Y., Ansell M. P., Dufresne A., Entwistle K. M., Herrera-Franco P. J., Escamilla G. C., Groom L., Hughes M., Hill C., Rials T. G., Wild P. M., 2001. Review Current international research into cellulosic fibers and composites, Journal of Materials Science 36, p. 2107.

[7] Oksman K., Mathew A. P., Långström R., Nyström B., Joseph K., 2009. The influence of fibre microstructure on fibre breakage and mechanical properties of natural fibre reinforced polypropylene, Composites Science and Technology 69, p. 1847.

[8] Zafeiropoulos N. E., Williams D.R., Baillie C.A., Matthews F.L., 2002. Engineering and characterization of the interface in flax fiber/polypropylene composite materials; Part I. Development and investigation of surface treatments, Composites: Part A 33, p. 1083.

[9] Zafeiropoulos N.E., Baillie C.A., Hodgkinson J.M., 2002. Engineering and characterization of the interface in flax fibre/polypropylene composite materials; Part II, The effect of surface treatments on the interface, Composites: Part A 33, p. 1185.

[10] Corrales F., Vilaseca F., Llop M., Girones J., Mendez J.A., Mutje P., 2007. Chemical modification of jute fibers for the production of green-composites, Journal of Hazardous Materials 144, p. 730.

[11] Soden P. D. &Hinton M. J., 1998. Predicting Failure in Composite Laminates: The Background to the Exercise, Composites Science and Technology 58, p. 1001.

[12] Gassan J., Bledzki A. K., 1999. Possibilities for improving the mechanical properties of jute/epoxy composites by alkali treatment of fibers, Composites Science and Technology 59, p. 1303.

[13] Mouton S., Teissandier D., Sébastian P., Nadeau J.P., 2010. Manufacturing requirements in design: The RTM process in aeronautics, Composites: Part A 41, p. 125.

[14] Maleque M. A., Belal F. Y., 2006. Mechanical properties study of pseudo-stem banana fiber reinforced epoxy composite, The Arabian Journal for Science and Engineering 32(2B), p. 359.

[15] Costa M. L., Muller de Almeida S. F., Rezende M. C., 2005. Critical Void Content for Polymer Composite Laminates, American Institute of Aeronautics and Astronautics JOURNAL 43(6), p. 1336.

Available online at www.sciencedirect.com

SciVerse ScienceDirect

Procedia Engineering 00 (2012) 000–000

Procedia Engineering

www.elsevier.com/locate/procedia

5th BSME International Conference on Thermal Engineering

Molecular Dynamic Simulation of Graphene Reinforced Nanocomposites for Evaluating Elastic Constants

R. Rahman[a], A. Haque[a*]

Department of Aerospace Engineering and Mechanics, The University of Alabama, Tuscaloosa, AL 35487,USA

Abstract

The mechanical properties of graphene/cellulose (GC) nanocomposites have been investigated using molecular dynamics (MD) simulations. The influence of graphene concentrations and agglomeration on elastic constants is studied. A polymer consistent force field (pcff) is used in the analysis. An efficient time integration scheme was implied in calculating the force in each time step from the corresponding position and velocity of the atom. The GC nanocomposites system undergoes NVT (constant number of atoms, volume and temperature) and NPT (constant number of atoms, pressure and temperature) ensemble with an applied uniform strain during MD simulation. The stress-strain responses were evaluated for GC unit cell in order to study the effects of graphene concentrations and agglomeration on Young’s modulus. The results show significant improvement in Young’s modulus for the GC nanocomposites compared to neat cellulose. The MD simulation results show reasonable agreement with the micromechanics based model and available experimental data.

© 2012 The authors, Published by Elsevier Ltd. Selection and/or peer-review under responsibility of the Bangladesh Society of Mechanical Engineers

Keywords: Molecular Mechanics, Nanocomposites, Elastic Constants

---

Nomenclature

Vol	volume of the simulation box
m_I	mass of I^{th} atom
v_i^I	velocity of I^{th} atom in i^{th} direction
N	total number of atoms
r_{ij}^{IJ}	ij -component of distance between I^{th} and J^{th} atoms
f_{ij}^{IJ}	ij -component of force between I^{th} and J^{th} atoms.
$\sigma_{11},\sigma_{22},\sigma_{33}$	virial stress in axial directions
$\bar{\sigma}$	hydrostatic stress

---

* Corresponding author. Tel.: 1-205-348-2694
E-mail address: ahaque@ua.edu

1. Introduction

Polymer nanocomposites are known to exhibit enhanced mechanical properties compared to neat polymeric system [1]. The nanofiller material such as graphene with significantly high strength and stiffness is an attractive candidate for reinforcing conventional polymeric materials. Cellulose is a bio-polymer suitable for graphene based nanocomposites. It is renewable, biocompatible and available in abundant quantities in nature. The cellulose based nanocompostes have potential for environmental friendly structures, sensors, energy storage, smart textiles and biomedical applications. It has been observed that the properties of nanocomposites depend on many parameters relating structural configurations of their constituent materials at the molecular level. The dispersion, concentrations and geometric configurations of nanoparticles such as thickness and aspect ratio, positions of atoms and interactions at the interface during deformation process are critical controlling parameters for achieving desirable mechanical properties. As a result developing reliable computational tools are extremely important in order to understand the interactions of various molecular entities of nanocomposites.

Molecular dynamics (MD) simulation is a powerful tool for numerical experiments of nanocomposites [2-3]. One of the aims of atomistic simulation is to reproduce experiment to elucidate the invisible microscopic details and further explain the experimental results. The fundamental concept behind molecular dynamics is to apply Newton's equations of motion in solving multi-body interacting system (i.e. polymers, crystals, nanocomposites etc.). The molecular interactions are the vital parts in MD simulation. This is defined by an appropriate force-field. The key components of a force-field are bonded interactions and non-bonded interactions such as van der Waals force. This makes molecular dynamics simulation to be a primary tool in assessing mechanical properties of polymer nanocomposites. Hence, this work is primarily focused in studying elastic constants of graphene-cellulose nanocomposites using classical molecular dynamics (MD) simulation. The effects of graphene weight percentage, geometric configurations and dispersion on mechanical properties of graphene/cellulose nanocomposite are investigated using MD simulation. Later, MD simulated mechanical properties are compared with in-house experimental data.

2. Model development and calculation details

This work considers MD simulation for two types of graphene/cellulose systems. Firstly, the amorphous graphene/cellulose model considers the effects of graphene weight concentrations on elastic constants. Secondly, the graphene dispersion model is used to study graphene's dispersion and agglomeration effect. The molecular dynamics simulations were carried out using an open source code LAMMPS, developed by Sandia National Laboratory [4].

2.1. Graphene concentration models

Cellobiose is a repeat unit for long cellulose chain (Fig. 1). Twenty cellobiose units were used in constructing a long cellulose chain. Each cellulose molecule consists of 843 atoms [5]. Graphenes with hydrogen terminated ends (Fig.1) were embedded in cellulose system to generate graphene/cellulose (GC) amorphous unit cell. Amorphous unit cells were constructed with 1%, 3% and 5% graphene weight concentrations by using one, three and five graphene sheets in individual system.

The average density for all the amorphous systems was maintained within the range of 1.3 g/cc to 1.4 g/cc. This was carried out by changing number of cellulose molecules in individual system. The GC unit cell with type-a graphene consists of 11 cellulose molecules. Periodic boundary condition (PBC) was applied on each unit cell during the equilibration and deformation process. The details about each amorphous unit cell after equilibration are shown in Table 1.

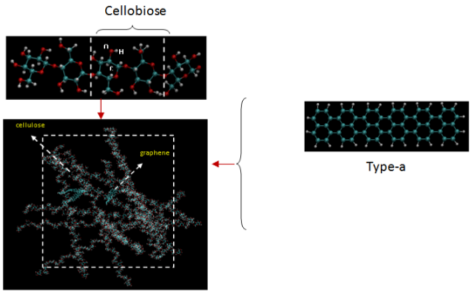

Fig.1. Graphenes embedded in cellulose matrix to form graphene-cellulose system

Prior to applying deformation, molecules in each unit cell were relaxed in order to attain minimum residual stress in the system. This was done by molecular mechanics approach while achieving minimum energy at stable structural configurations (i.e. bond, angle, dihedral etc). Conjugate gradient algorithm was used for 1000 steps with 10^{-8} kcal/mole energy tolerance [2]. Afterwards, the systems were equilibrated by isothermal-isobaric (NPT) molecular dynamics simulation for 3000 femtoseconds at 300 K temperature. At this stage, the system model was subjected to uniaxial deformation with 0.01% strain in every 0.1 picoseconds. The time step size varied within the range 0.3-0.7 femtoseconds. The atoms undergo isothermal molecular dynamics (NVT) for one picosecond after each deformation stage. A polymer consistent force field (*pcff*) was used in defining molecular interactions within the system [6].

The average stress was calculated throughout the whole unit cell by evaluating moving average of the virial stress, σ_{ij} defined by Equation (1). The first and second components of the virial stress are related to the kinetic and potential energy of the system, respectively [7].

Table 1. Details about graphene/cellulose amorphous unit cells

Material Configuration	Aspect ratio (AR)	Weight percentage of graphene	Unit cell dimension (A^0)
GC-I	AR-LW>=5, AR-LT>=150 (Type-a)	1%	a=b=c=47.39
GC-II	AR-LW>=5, AR-LT>=150 (Type-a)	3%	a=b=c=47.35
GC-V	AR-LW>=5, AR-LT>=150 (Type-a)	5%	a=b=c=48.70
	Neat Cellulose		a=b=c=16.00

$$\sigma_{ij} = -\frac{1}{Vol}\left[\left(\sum_{I=1}^{N} m_i \left(v_i^I v_i^{J^T}\right)\right) + \left(\sum_{I<J} r_{ij}^{IJ} f_{ij}^{IJ^T}\right)\right] \tag{1}$$

The developed stress in the system due to applied unidirectional strain is written in terms of average hydrostatic stress as

$$\bar{\sigma} = \frac{\left(\bar{\sigma}_{11} + \bar{\sigma}_{22} + \bar{\sigma}_{33}\right)}{3} \tag{2}$$

After every applied deformation, the running averaged hydrostatic stress $\bar{\sigma}$ is calculated in order to smoothen the stress-strain response. The Young's modulus is calculated from the slope of the linear regime of the stress-strain curve.

2.2. Graphene Dispersion Model

Three different GC models with single, agglomerated and dispersed graphene were constructed as shown in Fig. 2. The objective is to study the effects of single, dispersed and agglomerated graphene on the mechanical properties of GC system. Each GC unit cell contains 3% graphene with average density of 1.3-1.4 gm/cc. Unlike graphene concentration models, the graphenes reside among the amorphous cellulose with local order. All the unit cells were subjected to PBC as implied in graphene concentration model. A brief description of dispersion models is given in Table 2.

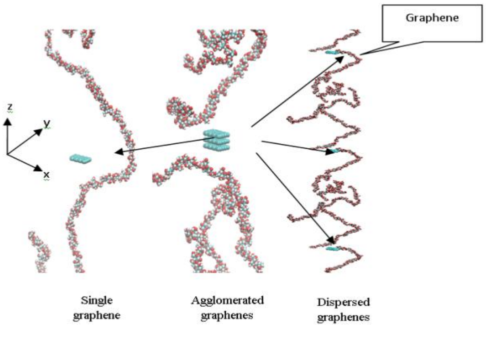

Fig. 2. Dispersion models of graphene-cellulose

Similar to graphene concentration models, the dispersion models were also equilibrated prior to applying deformation. Initially, optimum molecular configurations were achieved by minimizing the system energy based on conjugate gradient method for 1000 iterations. During energy minimization, the cell dimensions in x, y and z directions were also adjusted. Then, the systems were relaxed by isothermal-isobaric (NPT) molecular dynamics for 30000 steps with average step size of 0.5-1.0 femtoseconds. This was followed by deformation in x, y and z directions separately. The average applied strains were 0.001% along z-direction and 1% along x and y directions. After each deformation, the atoms were subjected to isothermal (NVT) molecular dynamics for 100 steps with time step size of 0.5-1.0 femtoseconds. After every applied deformation the running averaged hydrostatic stress $\overline{\sigma}$ was calculated using Equation. (2). The Young's modulus was obtained from the slope of the linear regime of the stress-strain curve.

Table 2. Unit cell configuration for dispersion models

Configuration	**Unit cell dimension (A^0)**	**Number of graphene plates**
S-CRYS-GnC-I	a=9.84, b=19.02, c= 354.87	1
S-CRYS-GnC-II	a=9.84, b=19.02, c=557.35	3 (Dispersed)
S-CRYS-GnC-III	a=9.84, b=19.02, c=1063.94	3 (Agglomerated)

3. Results and discussion

3.1. Effects of graphene concentrations on stress-strain response

In Fig. 3, the stress-strain responses of GC systems with various graphene concentrations are plotted. The Youngs modulus calculated from these plots are provided in Table 3. It is clearly observed from the slopes of stress strain plots in Fig. 3 that graphene enhances Young's modulus of cellulose based nanocomposites compared to neat cellulose. Fig. 3 shows increased Young's modulus of GC system with increased weight concentration of graphene (type-a, AR=150) in the range 1% to 5%. It is seen in Table-4 that the Young's modulus of neat cellulose is 11.93 GPa where as GC systems show the corresponding values 12.77 GPa, 20.63 GPa and 25.70 GPA with 1%, 3% and 5% graphene concentration, respectively. So, the results show more than 100% enhancement of Young's modulus with 5% nanographene reinforcement. The MD simulation based stress-strain data was compared with in-house tensile test data. The graphene weight percentages in these samples were slightly different from those of MD simulated test samples. In the experiments, 1.2%, 2% and 5% of graphene was used in preparing graphene/celllose system. These data show a reasonable agreement with the Young's modulus calculated from MD simulation as shown in Table 3. The experimentally obtained Young's modulii have increasing trend with respect to increasing weight percentage of graphene. This trend was also noticed in Young's modulus obtained from MD simulation. The linearly elastic region of stress-strain data in tensile test showed a reasonable resemblance with the simulated stress-strain response in MD simulation.

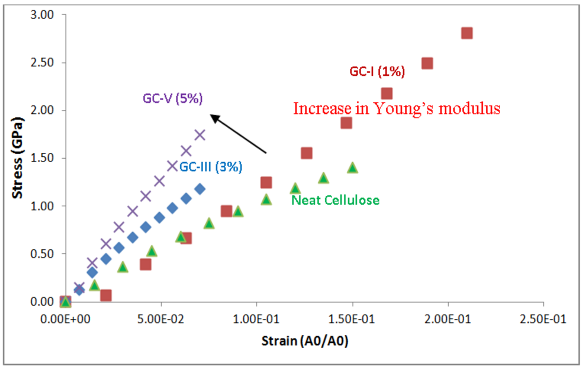

Fig. 3. Stress-strain response of graphene/cellulose systems with type-a graphene

3.2. Effects of graphene dispersion on stress-strain response

Dispersion model was used in studying the effect of agglomeration on mechanical properties of graphene/cellulose nanocomposites. Fig. 4-6 show MD simulated stress-strain responses in x, y and z direction of single, dispersed and agglomerated GC models as shown earlier in Fig. 2. In this case, x and y represent graphene length and width direction and z corresponds to thickness direction. The strain was applied independently in x, y and z direction. It is seen that stress generated in z direction is significantly low compared to x and y direction for all three cases. This occurs because stress in thickness direction is mostly matrix dominant whereas in plane properties are controlled by stronger reinforcing graphene. The variations in stress-strain responses in x and y direction as seen in Figs. 4-6 are due to different graphene length to width ratio and variable cell size used in these models.

Table 3. Calculated Young's modulus for amorphous graphene/cellulose systems

		Theoretical results		**Experimental results**		
Material Configuration in MD simulation	**Aspect ratio (AR)**	**Weight percentage of graphene**	**Young's modulus (GPa)**	**Material Configuration in tensile tests**	**Weight percentage of graphene**	**Young's modulus (GPa)**
GC-I	AR-LW>=5, AR-LT>=150	1%	12.77	Exp-G-C-Nc-I	1.2%	14.75±1.84
GC-IIII	AR-LW>=5, AR-LT>=150 (Type-a)	3%	20.63	Exp-G-C-Nc-II	2%	16.57±2.06
GC-V	AR-LW>=5, AR-LT>=150 (Type-a)	5%	25.70	Exp-G-C-Nc-III	5%	18.39±3.83
	Neat Cellulose		11.93 10.42		14.13±1.28	

Table 4 shows Young's modulus of single, agglomerated and dispersed graphene system calculated from stress-strain responses in x, y and z directions. It is evident that in plane Young's modulus, E_x and E_y for the dispersed system (11.78 GPa, 32.00 GPa) is comparatively higher than the same in agglomerated system (11.72 GPa, 21.81 GPa). It is to be noted that higher modulus was observed in graphene width direction rather than length direction. As a result well dispersed graphene with high aspect ratio is observed to provide improved in-plane Young's modulus. It is noticed that in-plane modulus in three agglomerated graphene based system is comparatively larger than single graphene system. This indicates that in-plane modulus is significantly influenced by graphene volume fraction since graphene's in-plane property is significantly high (Young's modulus, approximately 1 TPa). However, the out of plane Young's modulus, E_z of the GC nanocomposites is mostly controlled by E_z of matrix and van der waals interaction between graphene-cellulsoe or graphene-graphene. The results show lowest E_z value (0.07 GPa) for three layer dispersed graphene system whereas highest E_z value (2.81 GPa) was provided by three layer agglomerated system. The single layer graphene system shows E_z equals to 0.08 GPa. In agglomerated system, strong van der walls interaction between graphene-graphene possibly results such increased Young's modulus. It can be concluded from this study that graphene dispersion plays a vital role in controlling mechanical property in graphene based nanocomposites.

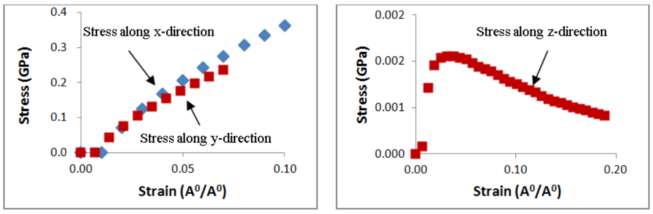

Fig. 4. Stress-strain response of semi-crystalline model with single graphene

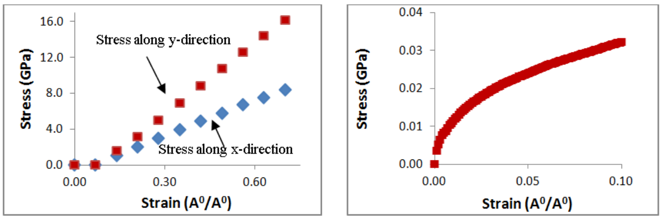

Fig. 5. Stress-strain response of semi-crystalline model with three agglomerated graphenes

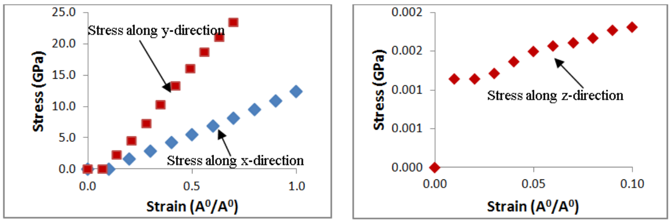

Fig. 6. Stress-strain response of semi-crystalline mode with three dispersed graphenes

Table 4. Young's modulus calculated from stress-strain response for semi-crystalline model

Configuration	**Number of graphene plates**	**E_x (GPa)**	**E_y (GPa)**	**E_z (GPa)**
S-CRYS-GnEp-I	1	4.04	3.63	0.08
S-CRYS-GnEp-II	3 (agglomerated)	11.72	21.81	2.81
S-CRYS-GnEp-III	3 (dispersed)	11.78	32.00	0.07

4. Conclusion

A molecular modelling frame work has been developed in order to determine Young's modulus of graphene/cellulose nanocomposites. The effects of graphene weight concentrations and dispersion have been studied. The Young's modulii of GC nanocomposites are seen to be comparatively higher than those of neat cellulose resin. The graphene concentrations in the range of 5% provided significantly improved Young's modulus. The Young's modulus determined by molecular modelling shows a reasonable agreement with the experimental results although slight discrepancy was observed. It is observed that dispersed graphene provides improved in-plane Young's modulus in comparison to agglomerated graphene system. The out of plane modulus in aligned (unidirectional) GC system is significantly low compared to in plane modulus in x and y direction.

Acknowledgements

The authors would like to acknowledge the support of this work by Alabama NSF EPSCoR grant.

References

[1] A. Haque, M. Shamsuzzoha, F. Hussain and D. Dean, 2003, S2-Glass/Epoxy Polymer Nanocomposites: Manufacturing, Structures, Thermal and Mechanical Properties", Journal of Composite Materials, 37 (20) p. 1821-1837
[2]Leach. Andrew, R. Molecular Modelling: Principles and Applications 1997, *Addison Wesley*
[3] Amnaya P. Awasthi, Dimitris C. Lagoudas, Daniel C. Hammerand. 2009, Modeling of graphene–polymer interfacial mechanical behavior using molecular dynamics", *Modelling and Simulation in Materials Science and Engineering*, 17, p. 015002
[4] http://lammps.sandia.gov/
[5] Wei Chen, Gary C. Lickfield, Charles Q. Yang, 2004, Molecular modeling of cellulose in amorphous state. Part I: model building and plastic deformation study, *Polymer*, 45, p**.** 1063-1071
[6] Sun H. 1998, Compass: An ab initio force field optimized for condensed phase applications – Overview with details on Alken and Benzene compounds, *Journal of Physical chemistry .B* 102(38), p. 7338-7364
[7] Zhu R., Pan E. and Roy A.K. 2007, Molecular dynamics study of the stress-strain behavior of carbon-nanotube Epon 862 composites, *Materials science and engineering A*. 447, p. 51-57

Available online at www.sciencedirect.com

SciVerse ScienceDirect

Procedia Engineering 00 (2012) 000–000

Procedia Engineering

www.elsevier.com/locate/procedia

5th BSME International Conference on Thermal Engineering

Degradation behavior of natural fiber reinforced polymer matrix composites

Takian Fakhrul[a], M.A Islam*

Department of Materials and Metallurgical Engineering,Bangladesh University of Engineering and Technology,Dhaka-1000,Bangladesh

Abstract

Nowadays, polyethylene (PE) and polypropylene (PP) based plastic materials are being extensively used for commercial and household purposes. However, these polymer based plastics are substantially resistant to biodegradation. Thus their increasing accumulation in the environment is proving to be an ecological threat to the world. Consequently, over the last couple of decades exhaustive studies on the biodegradation of plastics have been carried out in order to overcome the environmental problems associated with synthetic plastic waste. In this research, the improvement in the biodegradability of PP was observed by blending it with small additions (5%) of wood sawdust and wheat flour. The developed composites were then exposed to various environmental conditions namely; exposure to the open atmosphere, moist soil, water and brine solution for a period of 15 weeks. After exposure, the composites were visually inspected to find signs of crazing and discoloration that indicated the onset of biodegradation. The extent of the biodegradability of the composites was also observed by change in bonding nature by FTIR spectroscopy. In addition, the change in tensile properties of the composites after exposure was measured by tensile tests. The experimental results revealed that addition of both sawdust and wheat flour considerably improved the biodegradability of PP. The most pronounced biodegradation was exhibited by samples exposed to brine solution and those buried under moist soil.

© 2012 The authors, Published by Elsevier Ltd. Selection and/or peer-review under responsibility of the Bangladesh Society of Mechanical Engineers

Keywords: PP; natural fibers; composites; biodegradation; tensile properties.

1. Introduction

With advances in technology and increase in the global population, plastic materials have found wide applications in every aspect of our lives. Hence to meet these growing demands, approximately 140 million tonnes of synthetic polymers are being produced worldwide every year [1]. However, the most conventional plastics such as PE, PP, polystyrene, polyvinyl chloride and polyethylene terephthalate are non-biodegradable and continue to build up in the surroundings at a rate of 25 tonnes per year [1-4]. These plastics persist in landfills and in the environment where they are inadvertently ingested by animals and are making their way up the food chain proving to be a major ecological and environmental problem [4-9].

On the basis of these problems, an intensive activity has been undertaken since the early 1990s to develop novel plastics which have performance comparable with that of conventional polymers, but are also susceptible to microbial degradation [1-9].The intention was that these materials would reduce waste deposit volume while undergoing degradation in a landfill, or alternatively they could be treated in composting plants[1, 10].

In recent years, the incorporation of lignocellulosic materials in biodegradable matrices has become the subject of considerable research and effort [10-18]. Lignocellulosic and starch rich materials appear to be a suitable filler for biodegradable matrices exhibiting attractive properties such as low cost, low density, abundance, renewability and biodegradability [4,14-19].

Throughout the course of this research work, PP has been used as the synthetic polymer matrix, whose biodegradability has been tested by blending with flour (starch) and sawdust (cellulose). The composites were then exposed to four degradation conditions: (1) Moist soil to analyze the combined effect of microbial attack, oxidation and hydrolysis. (2) Water to analyze the combined effect of hydrolysis and oxidation. (3) 10% salt solution to examine the effect of chloride ion on degradation. (4) Normal environmental conditions (weathering) to examine effect of exposure to sunlight (UV, visible, and near infrared rays), moisture (humidity and rainfall), temperature cycling and wind.

After exposure to the degradation conditions for a period of 15 weeks, the biodegradability of pure PP and the developed composites was measured by visual inspection, tensile tests, FTIR analysis and water absorption tests. Moreover, SEM analysis of the tensile fracture surfaces was performed to determine the nature of failure.

2. Experimental

2.1. Materials

Commercial PP, bought from the local market in Dhaka, was used as the polymer matrix. The PP in the form of homopolymer pellets had a specific gravity of 0.91.The wood sawdust (mesh 80-100) used was medium wood obtained from a local sawmill in Dhaka. The wheat flour (mesh 230-270) used was also of local grade. Moreover, polyester and methanol were also used during the composite preparation to ensure uniform and adequate mixing.

2.2. Natural fiber preparation

The sawdust and wheat flour were dried in a furnace at 80°C for 24 hours to remove moisture and any volatile impurities present.

2.3. Fabrication of pure PP,PP-wood sawdust composites and PP-wheat flour composites

The PP and the natural fibers (5% by weight) were vigorously mixed with polyester and methanol to obtain a uniform mixture. The mixture was then heated in the furnace at 110°C for 20-30 minutes to remove moisture adhering to the surface and finally hot pressed into sheets measuring 220 mm x 220 mm x 3mm according to the heating cycle shown in Fig 1. Identical pure PP sheets were fabricated using the same parameters.

2.4. Preparation of samples for exposure to degradation conditions

The sheets were then cut into 115mm x 20mm x 3mm weathering samples (Fig 2.) for exposure to the degradation conditions for a period of 15 weeks.

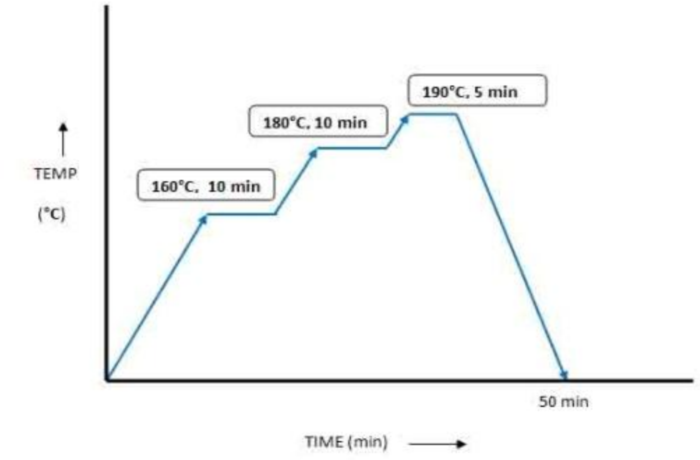

Fig 1.Heating cycle of hot press

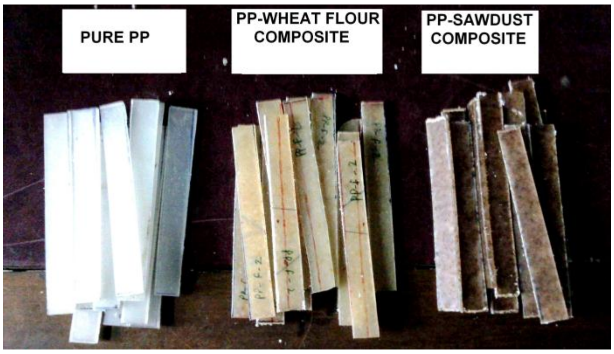

Fig 2. Samples prepared for weathering

`

2.5. Visual Inspection

After exposure to the degradation conditions all the samples were visually inspected and scrutinized to detect any indication of opaqueness and crazing that can directly be linked to the occurrence of surface degradation.

2.6. Fourier Transform Infrared Spectroscopy (FTIR)

The infrared spectra of the samples before and after exposure to the degradation conditions were obtained using a Nicolet 380 FTIR spectrophotometer. These were compared to determine the changes in chemical bonding nature after degradation.

2.7. Tensile Test

The tensile tests of the samples before and after exposure to the degradation conditions were carried out following the ASTM D638-01 [21] using a Universal testing machine of model INSTRON 3369 at a cross-head speed of 4mm/min. For each test, ten replicate samples were tested and the average values were reported.

2.8. Scanning Electron Microscopy (SEM)

The surface morphology of the fracture surfaces of the tensile specimens were examined by a scanning electron microscope. The samples were sputter coated with gold and observed at various magnifications ranging from 200 to 3000.

2.9. Water Absorption test

Samples made for water absorption testing were according to ASTM 570-98 [22]. The samples were first dried at 70^{o}C for 24 hours. The percentage of water absorption of pure PP and the composites were then calculated according to the formula;

$$\% \text{ Water Absorption} = \{(M_w - M_d) / M_d\}*100$$

where M_d is the weight of the samples before soaking in water and M_w is the weight after soaking in water for a period of one week.

3. Results and Discussion

3.1. Visual inspection results

After a period of 15 weeks of exposure in the degradation conditions, the samples were inspected thoroughly to find signs of crazing, heterogeneous surface erosion or discoloration that are a clear indication of surface degradation [5, 18-20]. The most marked crazing was observed in samples dissolved in brine (Fig 3.) and the least surface degradation was observed in samples exposed to atmospheric weathering. Moreover, the PP- wood sawdust composites showed most significant crazing in comparison to the PP- wheat flour composites which is apparent from Fig 3(a) and (b). The pure PP samples remained unaffected by any of the degradation conditions as shown in Fig 3 (c).

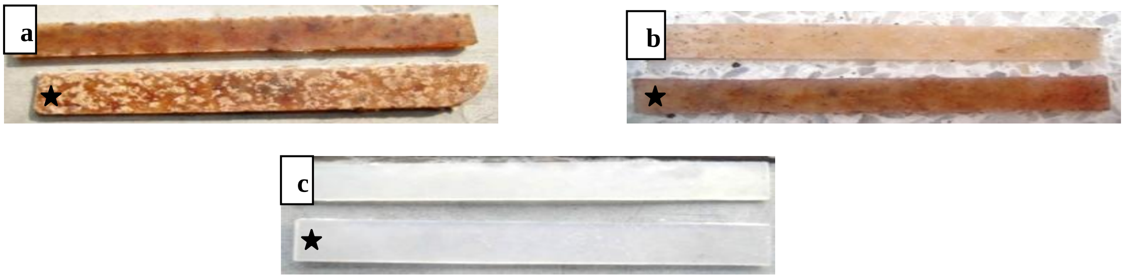

Fig 3 .Composite and pure samples before and after (star marked) exposure to brine solution for a period of 15 weeks have been compared here. (a) PP-sawdust composites, (b) PP-wheat flour composites and (c) pure PP samples.

3.2 Tensile test results

The tensile strength of the as-received pure PP was found to be 32.1MPa. However, addition of both wheat flour and sawdust to PP decreased its tensile strength to 29MPa and 26MPa respectively as confirmed by other researchers [14-18, 23]. This may be mainly attributed to the poor interfacial adhesion between the hydrophobic polymeric matrix of PP and the hydrophilic lignocellulosic fillers, which does not allow efficient stress transfer between the two phases of the material [14-18, 24]. The percentage elongation of both composites also decreased in comparison to pure PP.

Decrease in the tensile strength of the samples after exposure to the degradation conditions is a direct indication of the extent of degradation that has occurred. The most prominent decrease in tensile properties after degradation was observed in samples exposed to brine solution and those buried under moist soil and the least prominent decrease was observed in samples exposed to atmospheric weathering. Presence of chloride ion in brine is responsible for considerably weakening the composites and the presence of various soil microbes in soil facilitate biodegradation of the composites. Moreover, the PP-sawdust composites demonstrated a greater decrease in tensile properties than the PP-wheat flour composites in opposition to the tensile properties of the pure PP samples that remained almost unaffected by any of the degradation conditions. This is because sawdust contains highly hydrophilic substances like cellulose and hemicelluloses for which its water absorption ability is superior to wheat flour [18, 24]. Therefore, sawdust composites are more prone to biodegradation than wheat flour composites as they encourage and accelerate microbial attack and degradation by hydrolysis [1-2, 5, 18, 23]. The bar charts in Fig 5. and Fig 6. illustrate the changes in the tensile strength of the composites in the various degradation conditions.

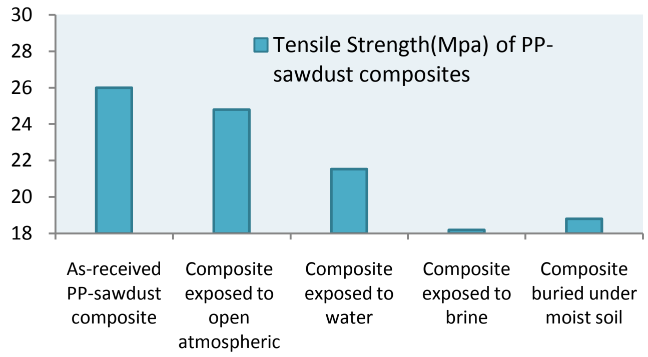

Fig 5. Bar chart showing the tensile strength of PP-sawdust composites after exposure to the degradation conditions

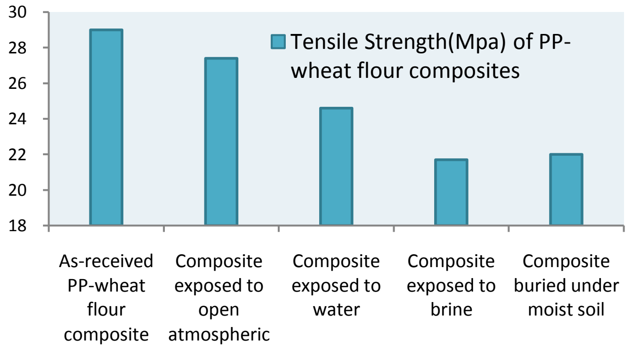

Fig 6. Bar chart showing the tensile strength of PP-wheat flour composites after exposure to the degradation conditions

.

3.3 SEM analysis

The SEM images of the tensile specimen fracture surfaces are shown in Fig 7. The fracture surfaces of pure PP are characteristic of a brittle fracture with cleavage planes (Fig 7a.).The fracture surface of both composites, especially the PP-sawdust composites, revealed the presence of voids (Fig 7b.) which clearly indicates the poor interaction between the non-polar matrix and polar fillers and thus explains the decreased tensile properties of the composites. Moreover, both composites revealed the presence of localized fibrils which suggest plastic deformation of the matrix as shown in Fig 7c. As the adhesion of the matrix and the fillers is poor so the matrix can deform independently until the filler particles restrict the deformation [16].

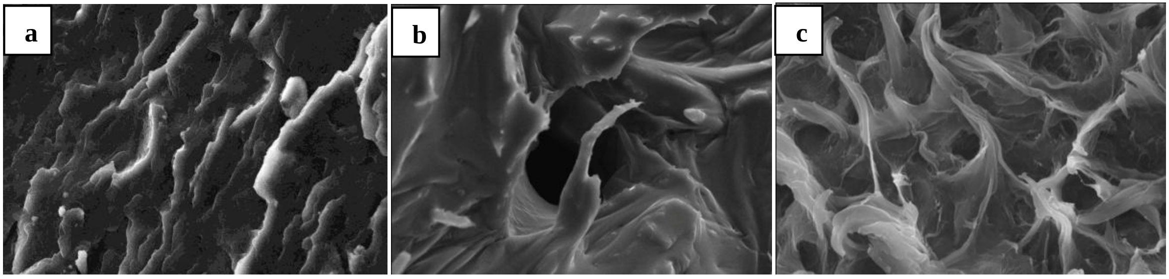

Fig 7: SEM micrographs showing fracture surfaces of (a) PP at a magnification of 1000x,(b) PP-sawdust composite at a magnification of 1000x, (c) PP-wheat flour at a magnification of 3000x

3.4 Water absorption test results

From the water absorption test results it is evident that pure PP is extremely hydrophobic and its water absorbing ability is significantly increased by the addition of sawdust and flour. Water absorption is higher in the PP-sawdust composite, i.e. almost twice as high, than the PP-flour composite. This may be attributed to the fact that wood is extremely hydrophilic in nature due to the presence of the hydrophilic hydroxyl groups of cellulose, hemicelluloses and lignin that responsible for water absorption [14,18,24]. This result also explains why the PP-sawdust composites exhibit more surface crazing and greater decrease in tensile properties than the PP-sawdust composites. The results are expressed in a bar chart in Fig 4.

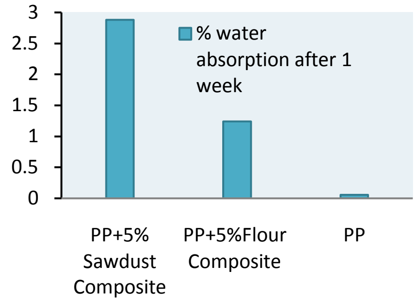

Fig 4. Bar chart showing percent water absorption of the samples

3.5 FTIR analysis

Analysis of FTIR spectrum of all the samples before and after exposure to the degradation conditions showed that the results were in parity with the tensile test and visual inspection outcome in which all the evidence pointed towards the fact that most degradation occurred in the sawdust composites exposed to brine followed by composites buried in moist soil.

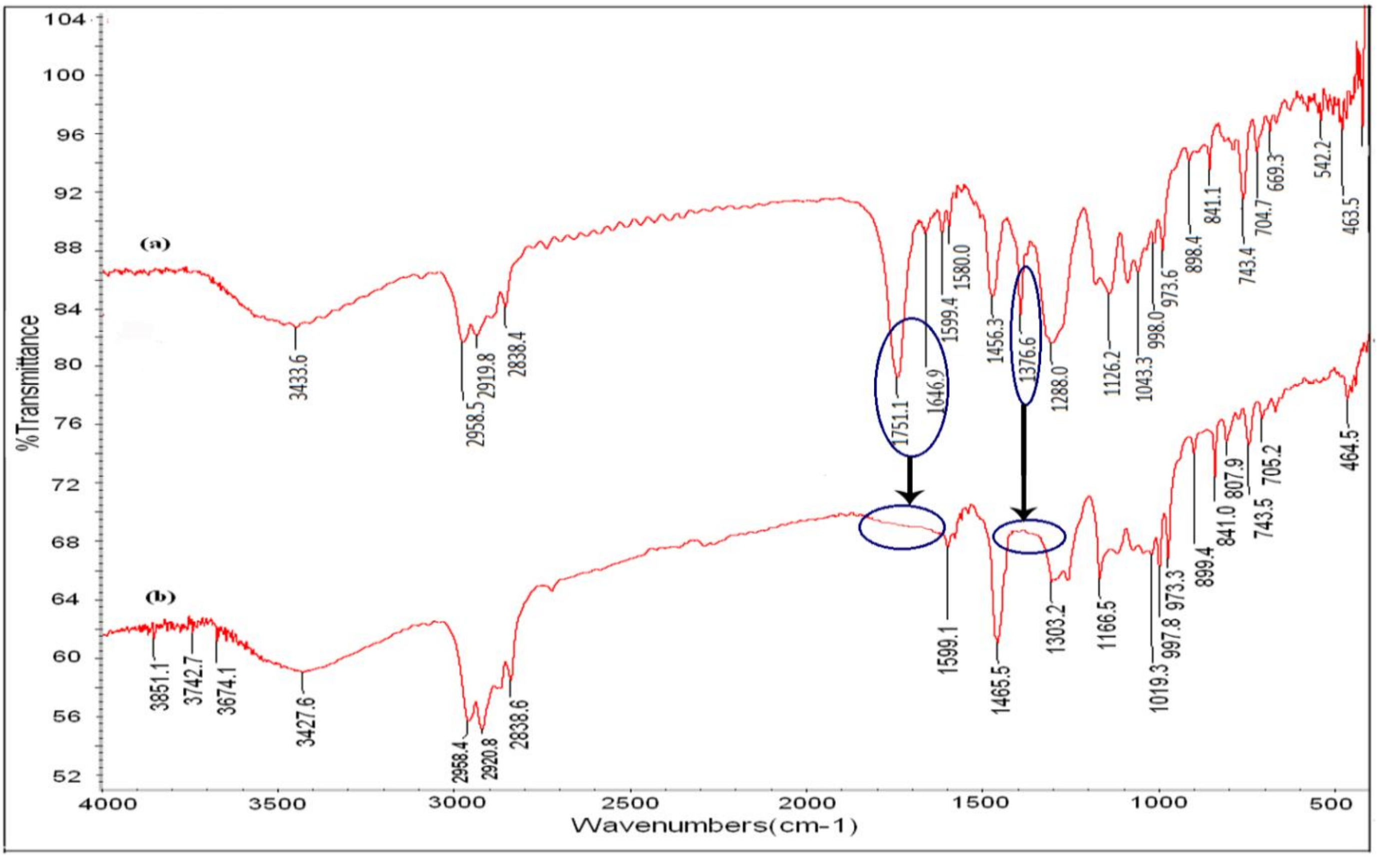

Fig 8. FTIR spectrum of PP-sawdust composite (a) before exposure, (b) after exposure to brine solution for 15 weeks

After exposure to the degradation conditions, the disappearance of functional groups determined by FTIR analysis indicates the dissociation or breakdown of the corresponding groups and thus gives an idea of the extent of degradation that has occurred [2, 5,13].The PP-sawdust composites exposed to brine solution revealed the disappearance of peaks at 1725cm^{-1}, 1646.9cm^{-1} and 1376.6cm^{-1}(Fig 8.) which positively indicates the dissociation of the bonds; carbonyl (C=O), carbon-carbon double bond (C=C) and methyl group (CH_3) respectively. Spectra of samples exposed to moist soil showed disappearance of peaks at 1725cm^{-1} and 1650cm^{-1}, whereas samples exposed to water revealed disappearance of the peak at 1725cm^{-1}and comparative attenuation in the intensity of the other peaks. The spectra of samples exposed to the open atmosphere showed the least changes. Furthermore, pure PP samples showed no visible changes in the spectra before and after exposure to any of the degradation conditions thus confirming the non-biodegradable nature of PP.

4. Conclusion

The addition of sawdust and wheat flour to PP has evidently increased its biodegradability which is apparent from the reduced tensile properties in the composites, the disappearance and attenuation of the infrared spectra peaks and visible crazing of the samples after exposure to the degradation conditions. The most pronounced degradation was observed in samples exposed to brine solution followed by samples buried under moist soil. This can be accounted for by the presence of the highly corrosive chloride ion in brine solution and the presence of microorganisms (bacteria and/or fungi) in the soil that initiate depolymerization on the surface of the composites thus aiding in the process of degradation. Composites exposed to water showed intermediate decrease in tensile properties and composites exposed to the open atmosphere showed the least decrease in tensile properties after exposure. Another interesting observation was that the PP-sawdust composites exhibited greater biodegradability than the PP-wheat flour composites which is because of the high water absorption ability of sawdust in comparison to wheat flour which facilitates an increased rate of degradation by microbial attack and hydrolysis.

References

[1] Premraj R and Mukesh Doble, “Biodegradation of Polymers”, Indian Journal of Biotechnology, Vol. 4, pp 186-193.

[2] J Arutchelvi, M Sudhakar, Ambika Arkatkar, Mukesh Doble, Sumit Bhaduri, and Parasu Veera Uppara,“Biodegradation of polyethylene and polypropylene”, Indian Journal of Biotechnology, vol. 7, pp 9-22.

[3] Pometto A L and Lee B,“Process of biodegradation of high molecular weight polyethylene by aerobic lignolytic microorganisms”, U S Pat5145779 8 08 Sept, 1992.

[4] M. Kolybaba1, L.G. Tabil, S. Panigrahi, W.J. Crerar, T. Powell and B. Wang, “Biodegradable Polymers: Past, Present, and Future”, proceeding of 2003 CSAE/ASAE Annual Intersectional Meeting.

[5] Hee-Soo Kim, Hyun-Joong Kim, Jae-Won Lee and In-Gyu Choi, “Biodegradability of bio-flour filled biodegradable poly (butylene succinate) bio-composites in natural and compost soil”, Polymer Degradation and Stability 91 (2006) 1117e1127.

[6] Franco CR, Cyras VP, Busalmen JP, Ruseckaite RA, Vazquez A., “Treated Degradation of polycaprolactone/starch blends and composites with sisal fibre”, PolymDegrad Stab 2004;86:95e103.

[7] Kim MN, Lee AR, Yoon SJ, Chin IJ, “Biodegradation of poly (3-hydroxybutyrate) Sky-Green and Mater-Bi by fungi isolated from soils”, Eur Polym J. 2000;36:1677e85.

[8] Okada M., “Chemical syntheses of biodegradable polymers”, Prog Polym Sci 2002;27:87e133.

[9] Wu CS., “Physical properties and biodegradability of maleated polycaprolactone/starch composite”,PolymDegrad Stab 2003;80:127 34.

[10] Md. Nazrul Islam and Md. Sakinul Islam, “Mechanical Properties of Chemically Treated Sawdust-Reinforced Recycled Polyethylene Composites”,Ind. Eng. Chem. Res. 2011, 50, 11124–11129.

[11] L. Averousand F. Le Digabel,“Properties of biocomposites based on lignocellulosic fillers”, Carbohydrate PolymersVolume 66, Issue 4, 23 November 2006, Pages 480 – 493.

[12] Ajay Karmarkar, S.S. Chauhan, Jayant M. Modakand Manas Chanda,“Mechanical properties of wood – fiber reinforced polypropylene composites: Effect of a novel compatibilizer with isocyanate functional group”,Composites Part A: Applied Science and ManufacturingVolume 38, Issue 2, February 2007, Pages 227 – 233.

[13] X. Ramis, A. Cadenato, J.M. Salla,, J.M. Morancho, A. Valle,L. Contat and A. Ribes,“Thermal degradation of polypropylene/starch-based materials with enhanced biodegradability”, Polymer Degradation and Stability 86 (2004), pp 483-491.

[14] Muhammad Abdul Mun’aim Mohd Idrus, Sinin Hamdan, Muhammad Rezaur Rahman and Muhammad Saiful Islam,“Treated Tropical Wood Sawdust-Polypropylene Polymer Composite: Mechanical and Morphological Study”, Journal of Biomaterials and Nanobiotechnology, 2011, 2,pp 435-444.

[15] Han-SeungYang, Hyun-Joong Kim et. al., “Rice-husk flour filled polypropylene composites; mechanical and morphological study”, Composite Structures 63 (2004) 305–312

[16] Hattotuwa G.B. Premalal, H. Ismail and A. Baharin,“Comparison of the mechanical properties of rice husk powder filled polypropylene composites with talc filled polypropylene composites”,Polymer Testing 21 (2002), pp 833–839.

[17] Md. Rezaur Rahman, Md. Nazrul Islam and Md. Monimul Huque, “Influence of Fiber Treatment on the Mechanical and Morphological Properties of Sawdust Reinforced Polypropylene Composites”, J Polym Environ (2010) 18, pp 443–450.

[18] V. Tserki, P. Matzinos, C. Panayiotou,“Novel biodegradable composites based on treated lignocellulosic waste flour as filler; Part II. Development of biodegradable composites using treated and compatibilized waste flour”, Composites: Part A, 37 (2006), pp 1231–1238.

[19] Joel R.Fried,"Polymer Science and technology", 2nd edition.

[20] Halina Kaczmarek, Dagmara Ołdak, Przemysław Malanowski and Hanna Chaberska,“Effect of short wavelength UV-irradiation on ageing of polypropylene/cellulose compositions”, Polymer Degradation and StabilityVolume 88, Issue 2, May 2005, Pages 189 – 198

[21] ASTM Standard D 638-01 (2002) Standard test methods for tensile properties of plastics.Annual book of ASTM Standard, vol 08.03.2002.

[22] ASTM Standard D 570-99 (2002) Standard test methods for water absorption of plastics. Annual book of ASTM Standard, vol 08.01.2002

[23] Da nutażuchowska, Ryszard Steller and Wanda Meissner, "Structure and properties of degradable polyolefin-starch blends", Polymer Degradation and Stability,Volume 60, Issues 2 – 3, 1998, Pages 471 – 480.

[24]Mohd Hafizuddin Ab Ghani and Sahrim Ahmad, "The Comparison of Water Absorption Analysis between Counterrotating and Corotating Twin-Screw Extruders with Different Antioxidants Content in Wood Plastic Composites", Advances in Materials Science and EngineeringVolume 2011, Article ID 406284, 4 pages.

`

Available online at www.sciencedirect.com

SciVerse ScienceDirect

Procedia Engineering 00 (2012) 000–000

Procedia Engineering

www.elsevier.com/locate/procedia

5th BSME International Conference on Thermal Engineering

Zn-doped SnO_2 with 3D cubic structure for humidity sensor

N.D. Md Sin[a] , Noorlaily Samsudin[b], S. Ahmad[c], M.H. Mamat[d], M. Rusop[e]

Faculty of Electrical Engineering, Universiti Teknologi MARA, 40450 Shah Alam, Selangor, Malaysia

[a]nordiyana86@yahoo.com, [b]noorlailysamsudin@yahoo.com, [c]samsiah81@gmail.com, [d]hafiz_030@yahoo.com, [e]rusop@salam.uitm.edu.my

---

Abstract

Zinc doped tin oxide (Zn-doped SnO_2) with three dimension (3D) cubic structure has been successfully grown on top of ZnO thin film. In this research, ZnO thin films prepared by rf magnetron sputtering and cubic structure of Zn-doped SnO_2 developed by immersion method at low temperature are reported. The effects Zn doping concentration at (0 to 5 at.%) on the Zn-doped SnO_2 were studied to form cubic structure. The performance of humidity sensor was tested using current-voltage (I-V) measurement (Keithley 2400) in a controlled chamber. The structural characterization was performed using field emission scanning electron microscopy (FESEM). The sensor performance at 5 % doping concentration was found to be highly sensitive and can be used as humidity sensor. The size of cubic structure decreases with the increase in doping concentration.

Keywords: *Zn-doped SnO_2; Three dimensional; Cubic structure; Humidity sensor; Sensitivity*

Nomenclature

RH%	Relative humidity percentage
S	Sensitivity
R_a	Resistance of the sensor in air
R_{rh}	Resistance of the sensor in the different RH%
at.%	Doping concentration
nm	Nanometre
V	Voltage
mL	Mililitre
°C	Degree celsius

1. Introduction

Performance of a sensor were always been an issue by major problems such as contamination, short life time, hysteresis and restricted to certain temperature and humidity [1-2]. There were various factors that influence the performance of sensor including morphology of structure as surface reaction, material as the medium of sensing and process preparation. Commonly, many researchers reported on one-dimensional (1D) nanostructures to fabricate devices structure for sensor application. However, three-dimensional (3D) nanostructure has received a positive observation among researchers for beneficial in physical and chemical properties [3]. Numerous materials were used as humidity sensor such as SnO_2 [4], ZnO [5] and TiO_2 [6]. The sensing performance of sensor material can be improved by doing some modification by doping with metal such as Al-doped ZnO[7], Ce doped SnO_2[8] and Pd doped SnO_2 [9]. The improvement of the sensor could be increased by two or more components of material [1]. Many researchers reported on composite ZnO-SnO_2 for gas sensor, but less for humidity sensor. These two materials were widely used for sensor due to their superior sensor properties. Various preparations for Zn-doped SnO_2 include sol-gel [10], sputtering [11], and hydrothermal [12]. In this research Zn was the minority carrier and Sn was the majority carrier. Due to the advantages of SnO_2 in terms of sensing properties the detection of reducing gases was based on a reaction between the semiconductor and the gas ambient which produces conductance changes in the conductivity of the semiconductor.

This was first time work that had been reported. The synthesis of $ZnSnO_3$ cubic structure for humidity sensor by hydrothermal method with size of cubes were about 200-400 nm [13]. The objective of our work was to study the effect of Zn doping concentration on the properties of Zn-doped SnO_2 that growth on ZnO catalyst by sol-gel immersion method for humidity sensor applications.

2. Methodology

ZnO thin films were deposited on glass substrates by radio frequency (RF) magnetron sputtering using SNTEK model. ZnO with high purity (99.999%) was used as target. Then, a sol-gel solution was prepared to deposit on top of ZnO thin film The experimental detail of the sol-gel solution preparation were explained; 0.02M tin(IV) chloride pentahydrate ($SnCl_4.H_2O$) (sigma-Al drich 98%) used as precursor and 1.3M sodium hydroxide (NaOH) (R&M Chemical) as mineralizer. $SnCl_4$ and NaOH were stirred in 50 mL deionised (DI) water respectively for 10 minutes. Then, $SnCl_4$ solution was taken and slowly dropped into NaOH solution under magnetic stirring. The amounts of dopant source, $ZnCl_2$ were controlled to achieve 0, 1.5, 3, 4, and 5 at% doping concentration in the SnO_2 solutions under stirring. Then, the solution was sonicated by ultrasonic for 10 minutes at 50°C to obtain white solution. Lastly, the white solution was transferred into containers that contain the sample of ZnO thin film. Then, the containers were immersed inside the water bath with 95°C DI water inside for 6 hours. After deposition of Zn-doped SnO_2 cubic structure, the final products were washed in distilled water and dried sample at 100°C for 10 minutes after deposition. Finally, the samples were annealed in the furnace at 500°C for 1hour.

Sensor performances were measured using 2 probe I-V measurement (Keithley 2400) to study sensitivity, repeatability and stability inside a humidity chamber (ESPEC SH-261). The temperature was set at room temperature (25°C) while relative humidity (RH%) was varied in the range 40 to 90 RH%. The humidity sensitivity measurements were conducted for the fabricated device with Au as the metal contact. The metal contact was used to attract or transmit the signal efficiently from the thin film to external circuit at humidity atmosphere. The surface morphology of Zn-doped SnO_2 cubic structure was characterized using FESEM (JEOL JSM 6701F). The thickness was measured using VEECO/Dektak 150+.

3. Results and discussions

Fig. 1(a) and 1(b) shows current versus voltage (I-V) graph of Zn-doped SnO_2 cubic structure thin films for Zn doping concentration at 1.5 at.% and 5 at.% respectively at different RH%. It can be seen that the current intensity increase with the increasing of RH% due to more water vapour has been absorbed by Zn-doped SnO_2 cubic structure. The current flows with less resistance due to the existence of the water vapour thus more current can pass through the sample as the RH% increase. The value sensitivity was calculated by using following equation (1) [1]:

$$S = \frac{R_a}{R_{rh}} \qquad (1)$$

Where S is sensitivity, R_a is resistance of the sensor in air, and R_{rh} is resistance in the different RH%. Fig 1(c) indicates undoped SnO_2 and Zn-doped SnO_2 cubic structure thin films were linearly sensitive to humidity range (40-90%RH). From the graph, it can be seen that the sample with 5 at.% doping concentration Zn-doped SnO_2 cubic structure show the higher sensitivity with at low RH% $R_{40RH\%}= 4.16\text{x}10^7\Omega$ is 22.5 times than $R_{90RH\%} = 1.85\text{x } 10^6\ \Omega$ at high RH% while the undoped SnO_2 thin films exhibit the lowest sensitivity. The inert graph in Fig 1(c) show the average sensitivity of undoped SnO_2 and Zn-doped SnO_2 cubic structure thin films increase as the Zn at.% doping concentration increase. The sensors exhibit 0.35 $RH\%^{-1}$ for average sensitivity for 5 at.% doping concentration Zn-doped SnO_2 cubic structured. The slope of the sensitivity versus relative humidity depends on the changes of current. This shows that Zn-doped SnO_2 cubic structure materials have the ability to absorb water vapour from the surroundings. It shows that Zn-doped SnO_2 cubic structure can increase the sensitivity of the humidity sensor [14-15]. More changes of the current resulted in much bigger slope. This was due to high surface area of Zn-doped SnO_2 cubic structure. Fig 1(d) shows Zn-doped SnO_2 cubic structure

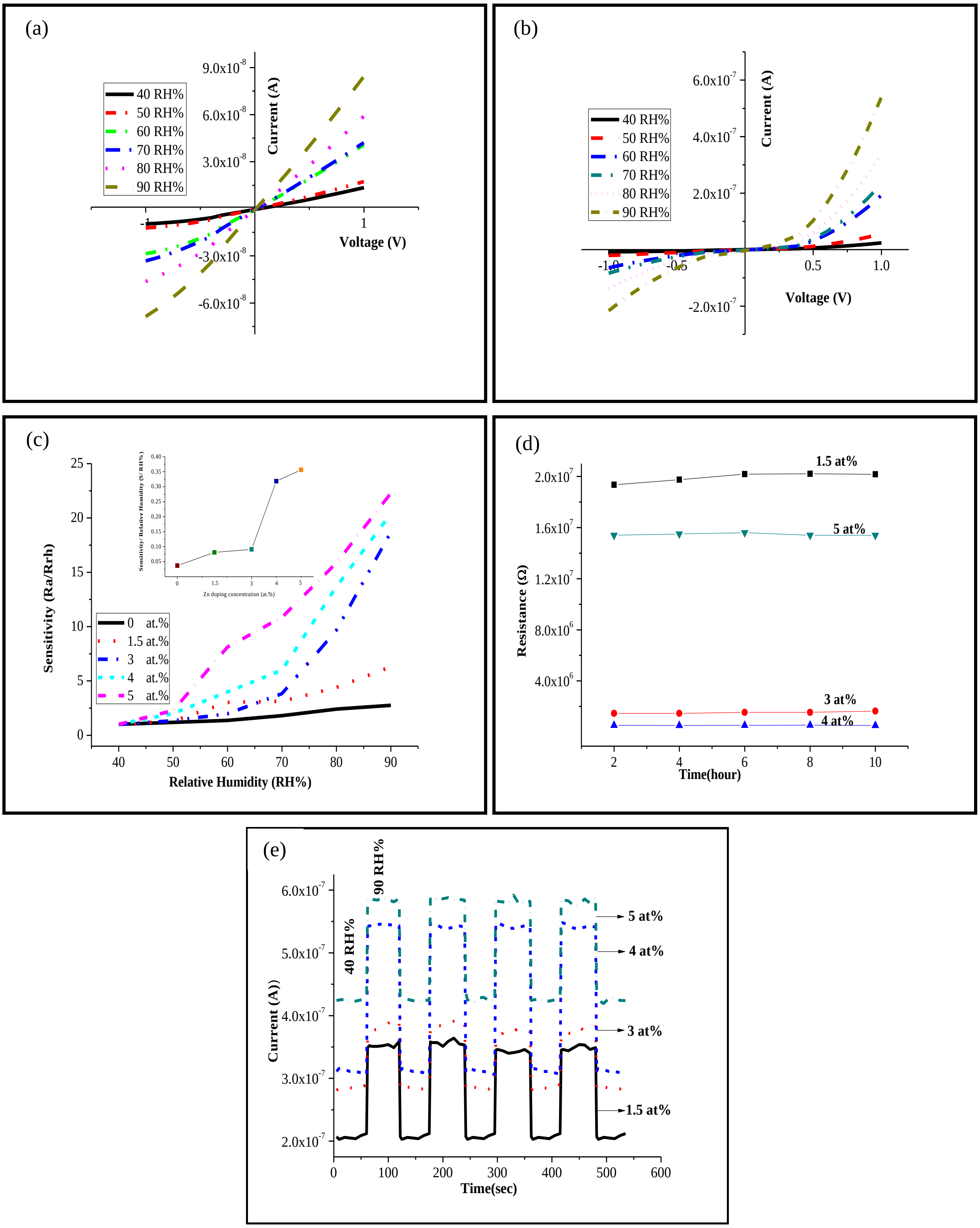

Fig. 1. I-V plot of (a)1.5 at.% and (b) 5 at.% doping concentration Zn-doped SnO$_2$ cubic structure at different RH% (c) sensitivity measurement of undoped SnO$_2$ and Zn-doped SnO$_2$ cubic structure thin films , (d) stability measurement of Zn-doped SnO$_2$ cubic structure thin films measured at 90 RH% with 1V applied for every two hours and (e) repeatability measurement measured at 90 RH% with 1V applied for 4 cycles for all sample.

thin films were good in stability which there were almost no changes of resistance during the measurement at 90 RH% condition for every two hours with supplied voltage 1 V. Fig 1(e) shows the repeatability of the sensor at 90 RH% at 1 V supplied voltage for 4 cycles. All sample show the repeatability characteristics which they have ability to reproduce the initial current during the humidity was high (90 RH%) and low (40 RH%). At high humidity (90 RH%)condition, the current of the samples increased rapidly when exposed to water vapour and then steadily reached at relatively stable value. When samples were exposed to dry air condition (40RH%), the current abruptly decreased and rapidly reached a relative stable value.

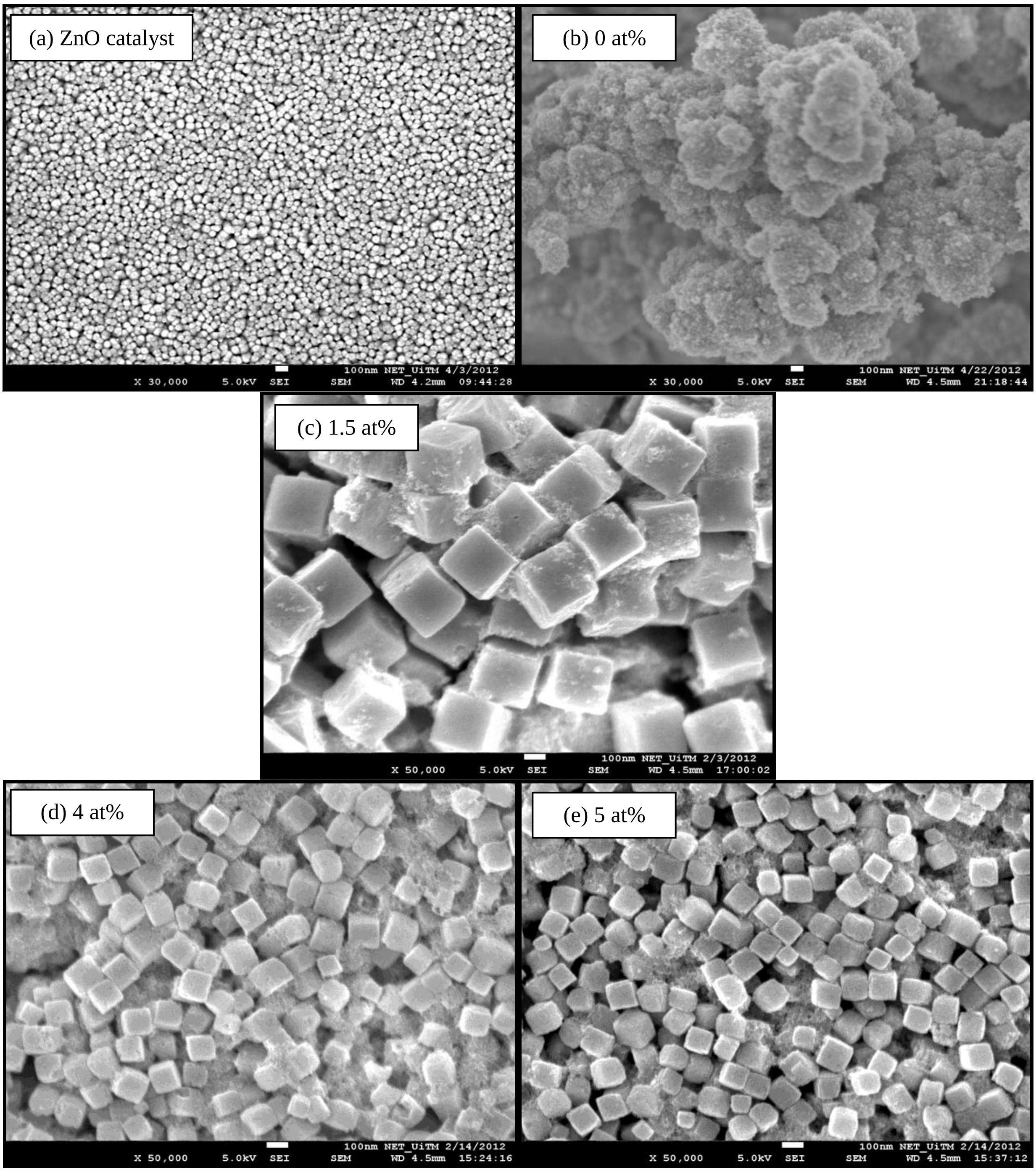

Fig. 2. FESEM image of (a)ZnO catalyst , (b) 0 at.% ,(c) 1.5 at.%, (d) 4 at.% and (e) 5 at.% doping concentration of Zn-doped SnO_2 cubic structure.

Fig. 2 (a) show the FESEM image of ZnO catalyst prepared by RF magnetron sputtering with size structure around 75-85 nm. The undoped SnO_2 (0 at.% doping concentration of Zn-doped SnO_2) particle structures as shown in Fig. 2(b). Fig. 2(c) show Zn-doped SnO_2 cubic structure and aggregation of amorphous nanoparticles of 1.5 at.% doping concentration with size of cubic structure 270 nm. Fig. 2 (d) and (e) show cubic structures of 4 at.% and 5 at.% doping concentration Zn-doped SnO_2 with size of cubic structure 134nm and 107nm respectively. The sizes of cube decrease as the doping concentration of Zn increase.

ZnO thin film acts as the template for the growth of Zn-doped SnO_2 cubic structure sol-gel solution. There were random aggregations of amorphous nanoparticles growth on the cube surface for all molar ratios as shown in Fig. 2 (b), (c) and (d). The aggregation of amorphous nanoparticles occurs due to surface tension and surface to-volume to ratio (Ostwald ripening law) [16-17]. The cubic structures were forming during the colloid particle that dissolves in DI water. The cubes crystallites size increase by the combination nanoparticles and the reaction temperature [18-19]. Due to the high surface area, 5 at.% doping concentration Zn-doped SnO_2 cubic structure performing the highest sensitivity to humidity since the cubic structured were the smallest due to the amount of oxygen vacancies and highly surface area lead to the increase in sensitivity due to more site area to absorb the water vapor [20].

Fig. 3(a) shows the surface morphology of 5 at.% doping concentration Zn-doped SnO_2 cubic structure. Fig. 3(b) shows the energy dispersive X-ray spectrum (EDS) of the cubic structure for 5 at.% doping concentration Zn-doped SnO_2. The peaks show the element that has been detected from the sample confirming that the presence of Zn, Sn and oxygen in thin film.

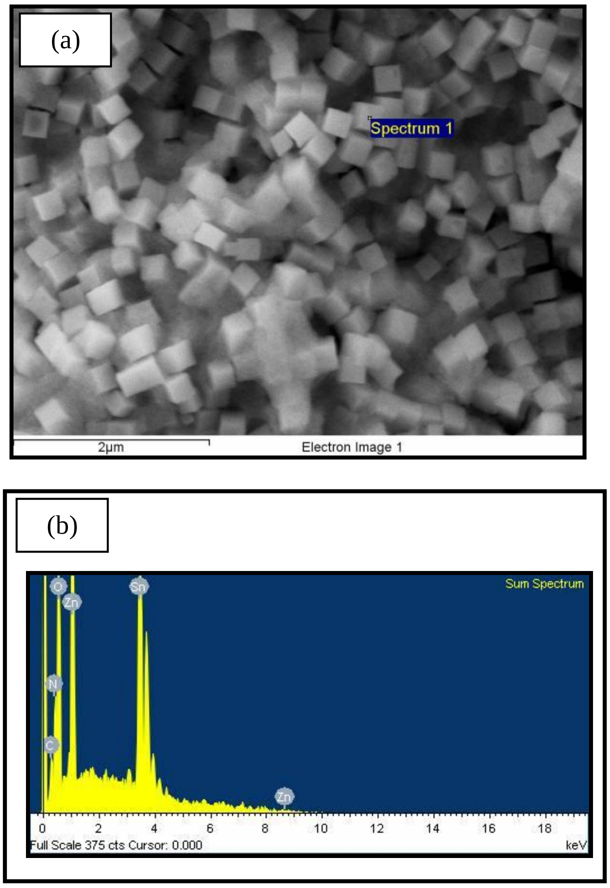

Fig. 3 (a) The surface morphology and (b) the EDS result of 5 at.% doping concentration of Zn-doped SnO_2 cubic structure.

4. Conclusions

Zn-doped SnO_2 cubic structures have been successfully deposited by using sol-gel immersion method on top of ZnO catalyst deposited by RF magnetron sputtering. From the I-V measurement, the current intensity increases proportionally with humidity due to existence of water vapour helps the current to flow. The sensitivity properties of 5 at.% doping concentration Zn-doped SnO_2 humidity sensor performs the highest at due to the higher surface area. Therefore, it is suitable for humidity sensor. The size of cubic structures Zn-doped SnO_2 reduces as the addition of Zn doping concentration increase. From the FESEM images, the size of the cubic structured of 5 at.% doping concentration Zn-doped SnO_2 was smaller compared to other parameters.

Acknowledgements

The author would like to express their thanks to Institute of Science and Faculty of Mechanical UiTM for providing the laboratory facilities. Thanks also to Research Management Institute (RMI) UiTM through the project 600-RMI/ST/DANA 5/3/Dst (392/2011) and Ministry of Higher Education (MOHE) for financial support.

References

[1] Z. Chen, C. Lu, “Humidity sensors: a review of materials and mechanisms”, Sens. Lett. 3 (2005) 274–295.
[2] Z.M. Rittersma, “Recent achievement in miniaturised humidity sensors – a review of transduction techniques”, Sensor and Actuators A 96 (2002) 196-210.
[3] Jiarui Huang, Kun Yu, Cuiping Gu, Muheng Zhai, Youjie Wu, Min Yang, Jinhuai Liu, “Preparation of porous flower-shaped SnO_2 nanostructures and their gas-sensing property” Sensors and Actuators B 147 (2010) 467–474.
[4] Qin Kuang,Changshi Lao, Zhong Lin Wang, Zhaoxiong Xie,and Lansun Zheng, “High-Sensitivity Humidity Sensor Based on a Single SnO2 Nanowire”, J. Am. Chem. Soc. 129 (2007) 6070-6071.
[5] Padmanathan Karthick Kannan, Ramiah Saraswathi, John Bosco Balaguru Rayappan,” A highly sensitive humidity sensor based on DC reactive magnetron sputtered zinc oxide thin film”, Sensors and Actuators A 164 (2010) 8–14.
[6] J.J. Steele, M.T. Taschuk, M.J. Brett,” Response time of nanostructured relative humidity sensors” Sensors and Actuators B 140 (2009) 610–615.
[7] N. D. Md Sin, M. Fuad Kamel, Rosalena Irma Alip, Zulfakri Mohamad, and M. Rusop , “The Electrical Characteristics of Aluminium Doped Zinc Oxide Thin Film for Humidity Sensor Applications“ Journal Advanced Materials Research and Engineering Vol. 364 (2012) pp 119-123
[8] Zhongwei Jiang, Zheng Guo, Bai Sun, Yong Jia, Minqiang Li, Jinhuai Liu, “Highly sensitive and selective butanone sensors based on cerium-doped SnO2 thin films” Sensors and Actuators B 145 (2010) 667–673.
[9] S. Harbeck, A. Szatvanyi, N. Barsan, U. Weimar, V. Hoffmann, “DRIFT studies of thick film un-doped and Pd-doped SnO2 sensors: temperature changes effect and CO detection mechanism in the presence of water vapour”, Thin Solid Films 436 (2003) 76–83.
[10] Marauo Davis, Walid M. Hikal, Cenk Gumeci and Louisa J. Hope-Weeks, “Aerogel nanocomposites of ZnO–SnO2 as efficient photocatalysts for the degradation of rhodamine B” Catalysis Science & Technology (2012).
[11] J.H. Ko, I.H. Kim, D. Kim, K.S. Lee, T.S. Lee, B. Cheong, W.M. Kim,”Transparent and conducting Zn-Sn-O thin films prepared by combinatorial approach”, Applied Surface Science 253 (2007) 7398–7403.
[12] Zhenhai Wen, Geng Wang, Wu Lu, Qiang Wang, Qian Zhang,and Jinghong Li,” Enhanced Photocatalytic Properties of Mesoporous SnO2 Induced by Low Concentration ZnO Doping”, Crystal Growth & Design Vol.7,NO.9 (2007) 1722-1725.
[13] Dipak Bauskara, B.B. Kaleb, Pradip Patil,’ Synthesis and humidity sensing properties of ZnSnO3 cubic crystallites’, Sensors and Actuators B 161 (2012) 396– 400.
[14] Rama Singh, Avadhesh Kumar Yadav, Chandkiram Gautam,” Synthesis and Humidity Sensing Investigations of Nanostructured $ZnSnO_3$” Journal of Sensor Technology 1 (2011) 116-124.
[15] Lijun Li, Ke Yu, Jin Wu, Yang Wang, and Ziqiang Zhu, “Structure and humidity sensing properties of SnO_2 zigzag belts”, Cryst. Res. Technol.45, No. 5 (2010) 539-544.
[16] Hai Fan, Shiyun Ai and Peng, “Room temperature synthesis of zinc hydroxystannate hollow core-shell microspheres and their hydrothermal growth of hollow core-shell polyhedral microcrystals”, CrystEngComm 13 (2011) 113.
[17] G.Jia , Y. Zheng, K. Liu, Y. Song, H. You, H.J Zhang, Phys. Chem. C 113 (2009) 153-158.
[18] Zhengjun Wang, Jie Liu, Feijiu Wang, Siya Chen, Hui Luo, and Xibin Yu, “Size-controlled Synthesis of ZnSnO3 cubic Crystallites at Low Temperature and Their HCHO-Sensing Properties”, J. Phys. Chem. C 114 (2010) 13577-13582.
[19] Sunandan Baruah and Joydeep Dutta “Zinc stannate nanostructures: hydrothermal synthesis”, Sci. Technol. Adv. Mater. 12 (2011) 013004 (18pp).
[20] Qin Kuang,Changshi Lao, Zhong Lin Wang, Zhaoxiong Xie,and Lansun Zheng, “High-Sensitivity Humidity Sensor Based on a Single SnO2 Nanowire”, J. Am. Chem. Soc.129 (2007) 6070-6071.

Available online at www.sciencedirect.com

SciVerse ScienceDirect

Procedia Engineering 00 (2012) 000–000

Procedia Engineering

www.elsevier.com/locate/procedia

5th BSME International Conference on Thermal Engineering

Prediction of electro-thermal responses of non-uniform functionally graded metal lines under a direct current field

A. K. Ghosh, Anik Adhikary, S. Reaz Ahmed*

Department of Mechanical Engineering
Bangladesh University of Engineering & Technology, Dhaka-1000, Bangladesh

---

Abstract

The electro-thermal response of thin, non-uniform functionally-graded metal lines subjected to a direct current flow is determined. The material properties associated with the problem are assumed to vary following a given functional relationship. The corresponding governing differential equations are derived in terms of variable electrical resistivity and thermal conductivity of the material. The solution of the boundary-value problem is then obtained numerically by using finite-difference technique. The electrical and thermal responses of a functionally graded metal line are presented in comparison with those of individual constituent metals. The results are claimed to be highly accurate and reliable, and are considered to be a valuable guide to thermal analysis of modern electronic devices.

© 2012 The authors, Published by Elsevier Ltd. Selection and/or peer-review under responsibility of the Bangladesh Society of Mechanical Engineers

Keywords: Electro-thermal problem, functionally graded material, non-uniform metal line, finite-difference technique.

Nomenclature

L, w, t	Length, width, thickness of line (m)	G	Volumetric heat generation ($\mathrm{Wm^{-3}}$)
A, C	Area ($\mathrm{m^2}$), perimeter (m)	A_m	Mechanical equivalent of heat ($\mathrm{Jcal^{-1}}$)
J	Current density ($\mathrm{Am^{-2}}$)	q	Thermal heat flux ($\mathrm{Wm^{-2}}$)
k	Thermal conductivity ($\mathrm{Wm^{-1}K^{-1}}$)	T	Temperature (K)
H	Convective co-efficient ($\mathrm{Wm^{-2}K^{-1}}$)	α	Material density ($\mathrm{Kgm^{-3}}$)
C_p	Specific heat capacity ($\mathrm{KJKg^{-1}{}^{\circ}C^{-1}}$)	ρ	Electrical resistivity (Ωm)
P	Electro-thermal heat flux ($\mathrm{Wm^{-2}}$)	φ	Electric potential (V)

1. Introduction

Accurate and reliable prediction of electro-thermal behavior of different conducting materials is of utmost importance for improved performance as well as integrity assessment of microelectronic devices. Now-a-days, it is of high practical importance to analyze these electro-thermal problems to determine the resultant temperature field properly. As a typical example of electro-thermal phenomenon, one can site electro-migration [1-2], which is the phenomenon of atomic diffusion due to current flow. When an electrical conducting material is subjected to a current flow, Joule heating is induced, which eventually leads to the generation of heat in the conductor. This electro-thermal conduction ultimately causes thermal stress in the materials, which is considered to be one of the major reasons of metal line failure in electronic packaging.

---

* Corresponding author. Tel.: +880-2-966 5636; fax: +880-2-861 3046.
E-mail address: srahmed@me.buet.ac.bd

The problem of heat conduction in a wire under the influence of current flow has been explained theoretically by Carslaw and Jaeger [3]. Steady temperature distribution near the tip of a crack in a homogeneous isotropic conductive plate was analyzed by Saka and Abe [4] under a direct current field with the help of path-independent integrals. Further, the analysis was extended by Sasagawa *et al*. [5] to determine the current density and temperature distributions near the corner of an angled metal line subjected to direct current flow. Greenwood and Williamson [6] treated the case of a conductor subjected to a direct current flow, in which temperature dependent material properties were considered. The method was further extended by Jang *et al*. [7] to give a general solution to the coupled nonlinear problem of steady-state electrical and thermal conduction across an interface between two dissimilar half spaces. Wang *et al*. [8] also presented analytical solutions for the electrical and thermal conduction near the tip of a crack with a constant flux boundary condition at an infinite region. The method of Greenwood and Williamson was also extended by Jang [9] to obtain a solution to the coupled nonlinear problem of steady-state electrical and thermal conduction across a crack in a conductive layer for which material properties were assumed to be functions of temperature. Recently, introducing a new Joule heating residue vector, heat conduction in symmetrical electro-thermal problems has been analyzed under the influence of direct current passing through symmetrical regions of the boundary [10]. A nonlinear analysis has also been reported for electro-thermal response of a metallic wire of dissimilar materials with temperature dependent thermal conductivity [11]. Very recently, the resulting temperature field of a 2D electro-thermal problem near the corner composed of two dissimilar materials in an angled metal line has been analyzed under a direct current flow by Saka and Zhao [12].

This paper presents a new analysis of a heat conduction-convection problem of a functionally graded metal (FGM) line coupled with an electrical problem subjected to a direct current field. The non-uniformity of the metal line is modelled by a typical converging-diverging shape with a variable rectangular cross section. The associated material properties, namely the electrical resistivity and thermal conductivity are assumed to vary as a function of spatial coordinate. The heat generated due to current flow is determined based on the resulting distribution of electric potential. The solution of both the boundary-value problems is obtained numerically using the finite-difference technique. The electro-thermal responses a non uniform FGM metal line are demonstrated in comparison with those of the individual constituent metal lines.

2. Mathematical formulation

2.1. Electrical problem

Ohm's law for one dimensional potential distribution,

$$\frac{d\,\varphi}{d\,x} = -\,\rho(x)\,J\,(x) \tag{1}$$

The differential equation that governs the distribution of electric potential within the material body can be obtained by applying divergence operator on Eq. (1), which eventually takes a form like

$$\frac{d^2\varphi}{dx^2} = -\left(\frac{d\rho(x)}{dx}\,J(x) + \rho(x)\,\frac{d\,J(x)}{dx}\right) \tag{2}$$

For uniform cross-sectional area and constant electrical resistivity, the derivatives in the right hand side of the Eq. (2) can be neglected. Equation (2) will then be reduced to the one dimensional Laplace's equation.

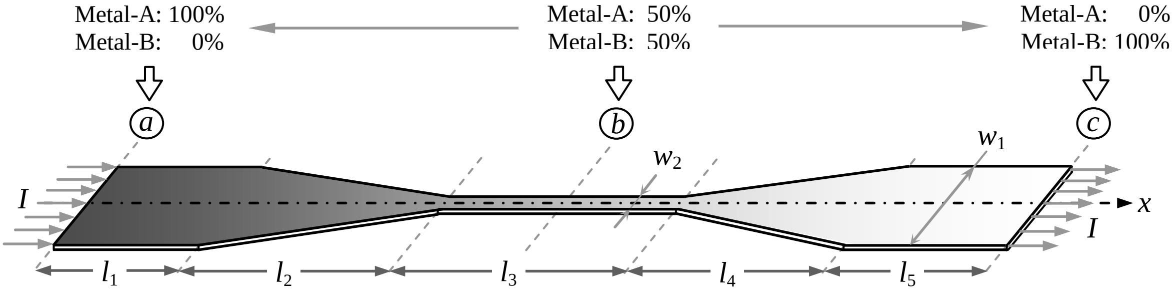

Fig. 1. Model of a non uniform thin functionally graded metal line under a direct current field

2.2. Thermal problem

The general governing equation for heat transfer in a metal line, the surface of which losses heat by convection to the surrounding atmosphere ($T_\propto$) is

$$\frac{1}{A(x)}\,\frac{\partial}{\partial x}\left[A(x)k(x)\frac{\partial T}{\partial x}\right]-\frac{H\,C(x)}{A(x)}[T-T_\propto]+G(x)=\alpha\,C_p\,\frac{\partial T}{\partial t} \tag{3}$$

For the present electro-thermal problem the internal heat generation per unit volume (*G*) is related to Joule heating caused by the current flow. For steady-state heat transfer with variable thermal conductivity *k*(*x*), subjected to Joule heating, the governing equation reduces to

$$\frac{1}{A(x)}\,\frac{d}{dx}\left[A(x)k(x)\frac{dT}{dx}\right]-\frac{H\,C(x)}{A(x)}\,[T-T_\propto]+\frac{1}{A_m\,\rho(x)}\left(\frac{d\varphi}{dx}\right)^2=0 \tag{4}$$

For the solution of electrical problem, the end conditions of the metal line are simulated by the following relations

$$\frac{d\varphi}{dx}=\pm\,\rho\,\left(\frac{I}{A}\right) \tag{5}$$

The negative sign of the equation (6) applies to the line end where current is being injected and the positive sign corresponds to the current outlet port. For the thermal problem, the temperatures at the two ends of the line are assumed to be known. It is however mentioned that all possible physical conditions at the ends can readily be accommodated.

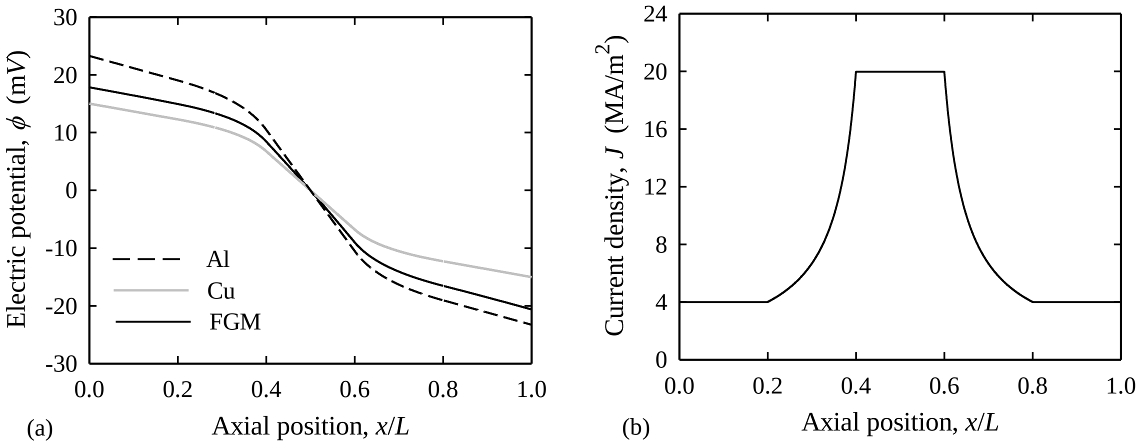

Fig. 2. Distributions of (a) electric potential and (b) current density along the non-uniform metal lines under I = 2 A

2.3. Electro-thermal heat flux

Electro-thermal heat flux of a conductive wire is realized as a summation of the thermal heat flux and the flux representing the effect of electrical heating in the wire. The overall heat flux vector (*P*) related to the coupled electro-thermal problem, which is also known as the Joule heating residue vector [7], is defined by

$$P(x)=-\,k(x)\;grad\left[T+\frac{\varphi^2}{2\,k(x)\rho(x)}\right] \tag{6}$$

Where, the first term in the right hand side of Eq. (7) is the thermal heat flux, $q=-k\;grad\,T$, and the second term reflects the corresponding effect of electrical heating.

3. Method of solution

The present steady state heat conduction-convection boundary-value problem has been solved numerically by using finite-difference technique. Both the governing differential equations associated with the electrical and thermal problems are discretized using the standard three-point central-difference scheme. The difference equations so developed for the electrical and thermal problems are respectively as follows:

$$\varphi_{i+1} - 2\varphi_i + \varphi_{i-1} = -\frac{h}{2}\left[J_i\left(\rho_{i+1} - \rho_{i-1}\right) + \rho_i\left(J_{i+1} - J_{i-1}\right)\right] \tag{7}$$

$$\begin{aligned}&[4k_i + k_i A_i^{-1}\left(A_{i+1} - A_{i-1}\right) + \left(k_{i+1} - k_{i-1}\right)]\,T_{i+1} - [8k_i + 4A_i^{-1} H\, C_i h^2]\,T_i + \\ &[4k_i - k_i A_i^{-1}\left(A_{i+1} - A_{i-1}\right) - \left(k_{i+1} - k_{i-1}\right)]\,T_{i-1} = -4A_i^{-1} H\, C_i h^2 T_\infty - \rho_i^{-1} A_m^{-1}\left(\varphi_{i+1} - \varphi_{i-1}\right)^2\end{aligned} \tag{8}$$

A MATLAB based computer code was developed to couple the electrical and thermal problems. The resulting tri-diagonal systems of algebraic equations are solved by the matrix decomposition method. For the calculation of secondary parameters of interest, namely current density, electrical heat generation, electro-thermal heat flux, etc., both the three-point forward and backward as well as central differencing schemes were adopted to keep the order of error the same (O(h^2)). A total of 1000 nodal points have been considered to descritize the computational domain. The convergence as well as the stability of the numerical solution has however been verified by varying the nodal points from 1000 to 7000.

Table 1: The assumed electrical resistivity and thermal conductivity of Copper and Aluminum at room temperature

Metal	Electrical resistivity (ρ) (Ω-m)	Thermal conductivity (k) (Wm^{-1}K^{-1})
Copper (*Cu*)	1.71×10^{-8}	423.60
Aluminum (*Al*)	2.65×10^{-8}	249.20

4. Statement of the electro-thermal problem

Figure 1 shows the analytical model of a variable cross-sectional metal line of FGM with overall dimensions, L = 200 mm, w_1 = 5 mm, w_2 = 1 mm, t = 100 μm under the influence of a steady direct current field. The FGM line is assumed to be composed of two metals (Cu and *Al*), the composition of which varies linearly over the length (x = 0 ~ L). The entire metal line is assumed to be electrically insulated except for the two ends. For the solution of electrical problem, in addition to the given current densities at the two ends of the line, the zero potential condition is also satisfied at its mid-length position.

As a result of current flow in the line, Joule heating occurs. Volumetric internal heat generation is calculated with the help of potential distribution as shown in Eq. (4). The temperature distribution of the FGM line largely depends on thermal conductivities of the constituent metals. The surface of the line is assumed to transfer heat by convection to the surrounding environment which is at a temperature of 318K. The elevated temperature condition of the wire was simulated by assigning fixed temperature (318K) at the two ends of the wire. The convection heat transfer co-efficient is assumed to be constant (10

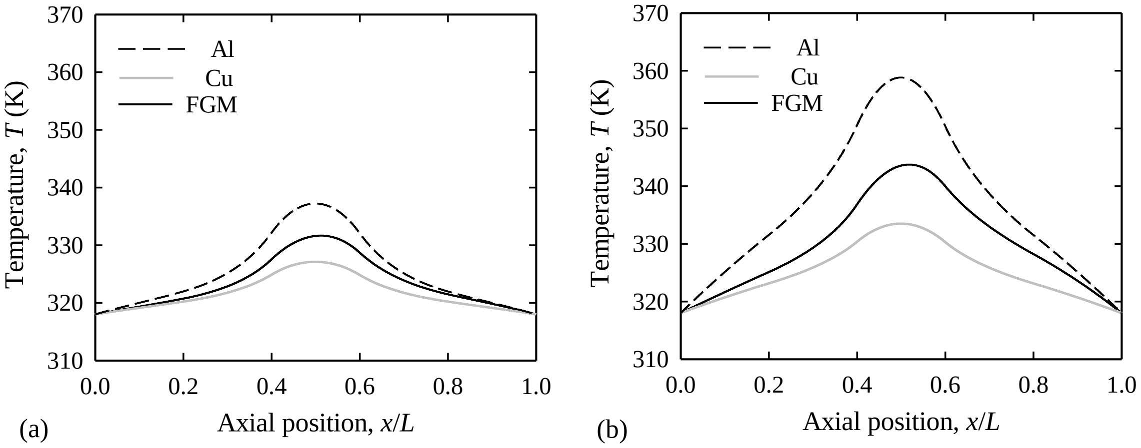

Fig. 3. Temperature distribution along the metal lines under I = 2A: (a) bare lines, (b) buried lines

$Wm^{-2}K^{-1}$) for the entire span of the FGM line. The individual electrical resistivity and thermal conductivity of the two constituent metals (*Cu* and *Al*) assumed for the present analysis are listed in Table 1. Both the material properties of interest are assumed to vary following a linear law along the length of the FGM line, which are as follows:

$$\rho(x) = \rho_{Cu} + (\rho_{Al} - \rho_{Cu})(x/L) \tag{9}$$

$$k(x) = k_{Cu} + (k_{Al} - k_{Cu})(x/L) \tag{10}$$

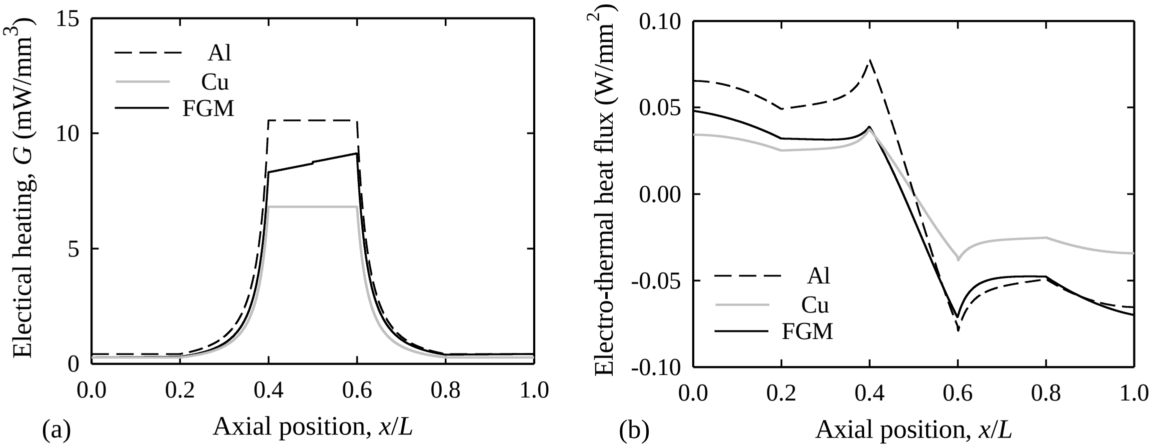

Fig. 4. Distributions of (a) heat generated and (b) electro-thermal heat flux along the non-uniform metal lines under $I = 2$ A

5. Analysis of the response

This section describes the electro thermal responses of a FGM metal line (*Cu-Al*) subjected to a direct current field. Fig 2 shows the variations of electric potential and the resulting current density along the axis of the FGM as well as the constituent metal lines. It shows that the electric potential varies linearly for uniform sections of the metal lines, while the same varies nonlinearly for sections having non-uniform cross-sectional area. The potential distribution for the FGM metal line resides in between those of the parent metals, and maintains higher similarities with that of *Cu* for the starting section and *Al* for the end section. This is because the proportion of *Cu* is higher for the first half section and *Al* is higher for the last half section. The electric potential for the FGM line is found to assume slightly different values for the two ends, although the distributions of individual *Cu* and *Al* lines are symmetric about their mid-length position.

Fig. 2(b) shows the distribution of current density, which is obtained by using Eq. (1) and the distribution of electric potential along the metal line. Now, since the current supply is kept constant, the distribution of current density, *J* depends only on the cross-sectional area (*I*/*A*). That is why the distributions of current density for all the three metal lines overlap on each other. Moreover, it is seen that the calculated current density distribution agrees very well with the actual current density, which, in tern, validates the present finite-difference solution for the electric problem.

Fig. 3 describes the variation of the resulting temperature along the metal lines under two different physical conditions, which are in fact bare and buried lines. In an attempt to compare the thermal response of FMG metal line with those of individual *Cu* and *Al* lines, the corresponding temperature distribution is presented together with those of the individual *Al* and *Cu* lines (see Fig. 3). For the individual metal lines, the distributions are found to be symmetric about the mid-length position, at which the maximum temperature is developed. However, this is not the case for the FGM line, in which the maximum temperature position is shifted slightly towards the right from its mid-length position. Fig. 3(b) describes the corresponding temperature profiles for the case of buried metal lines which are found to be very similar to those of bare lines in terms of nature of variation, but they differ quite significantly in the sense of magnitude. This is quite logical because, in case of buried lines, no heat loss is allowed from their surfaces through convection to surroundings, thereby shifting the overall state of temperature to a higher level compared to the case of bare lines.

The variation of heat generation and the electro-thermal heat flux vector is presented in Fig. 4 as a function of axial location of lines. It is revealed that the amount of electrical heating increases rapidly towards the mid-section of the metal lines from both ends. The numerical results are found to be in conformity with the expectation, because the area decreases to its minimum value at around the mid-section region of the line. Since the current density increases with the decrease of cross-sectional area, the amount of heat generation which is proportional to the current density, also increases around the mid section region and attains its highest value. The highest amount of heat is found to generate in *Al* line and the lowest in *Cu* line, while that of FGM line remains in between the two. It can be also mentioned that, for the areas with constant cross-section heat generation remains constants for individual metal lines, but varies linearly for the case of FGM line, which is mainly due to the change of material composition along the current flow path. Figure 4(b) shows the variation of the electro-thermal heat flux vector for the FGM as well as the constituent metal lines as a function of their axial location. The average value of the heat flux vector for the FGM line remains in between those of *Al* and *Cu* lines. The symmetry in the variation of the heat flux vector as observed for the case of individual metal lines, is found missing in the case of FGM line.

Fig. 5 describes the effect of electric field intensity on the electric potential and temperature fields of the FGM line. As expected, with the increase of field intensity, electric potential increases significantly but the nature of variation remains almost unchanged. The effect on the temperature distribution is identified to be more critical, as the maximum temperature increases to a very high level even with a relatively smaller change in the supplied current. A quantitative analysis shows that the increase in temperature in the FGM line is around 10 degrees, when the supplied current is changed from 1A to 2A only, and the corresponding change in temperature is 17 degrees when *I* changes from 2A to 3A (see Fig. 5(b)).

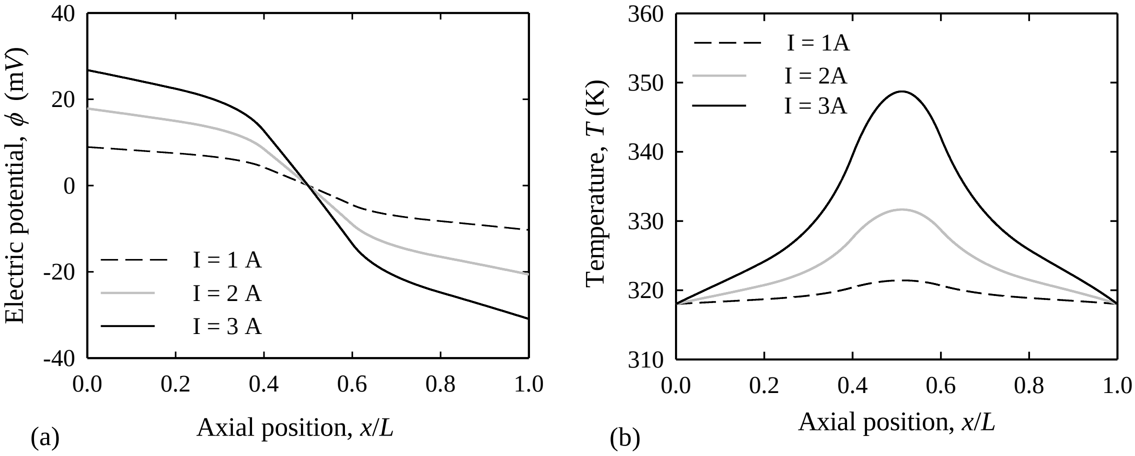

Fig. 5. Effect of electric field intensity on electro-thermal responses of FGM line: (a) electric potential, (b) temperature

6. Conclusions

Electro-thermal response of a thin, non-uniform FGM metal line is analyzed under the influence of a direct current field taking into account the associated material properties as a linear function of spatial coordinate. It is observed that the electric potential and temperature as well as their distributions over the FGM line differ significantly from those of the individual constituent metal lines. The effect of electric field intensity on the response of FGM line is identified to be quite substantial.

References

[1] Blech, I., A., 1976. Electromigration in thin aluminum films on titanium nitride, Journal of Applied Physics 47 (4), p. 1203-1208.
[2] Abé, H., Sasagawa, K., and Saka, M., 2006. Electromigration failure of metal lines, International Journal of Fracture 138 (1-4), p. 219-240.
[3] Carslaw, H., S., and Jaeger, J., C., 1959. Conduction of Heat in Solids, Second Ed., Clarendon, Oxford,
[4] Saka, M., and Abé, H., 1992. Path-independent integrals for heat conduction analysis in electrothermal crack problem, Journal of Thermal Stresses, 15 (1),p. 71-83.
[5] Sasagawa, K., Saka, M., and Abé,H., 1995. Current density and temperature distribution near the corner of angled metal line, Mechanics Research Communication, 22 (5), p. 473-483.
[6] Greenwood, J., A., and Williamson, J., B., P., 1958. Electrical conduction in solids, Theory of temperature-dependent conductors, Proc. Roy. Soc. Lond. A, 246(1244), p. 13-31.
[7] Jang, Y., H., Barber, J., R., and Hu, S., J. 1998. Electrical conductance between dissimilar materials with temperature-dependent properties, Journal of Physics D: Applied Physics, 31 , p. 3197-3205.
[8] Wang, P., Tian, Z., G., and Bai, X., Z., 2003. Electrothermal stress in conductive body with collinear cracks, Theoretical and Applied Fracture Mechanics, 40 (2) , p. 187-195.
[9] Jang, Y., H., 2005. Electro-thermal crack analysis in a finite conductive layer with temperature-dependent material properties, Journal of Physics D: Applied Physics, 38, p. 2468-2475.
[10] Saka, M., Sun, Y., X., and Ahmed, S., R., 2009. Heat conduction in a symmetric body subjected to a current flow of symmetric input and output, International Journal of Thermal Sciences, 48, p. 114-121.
[11] Rahman, S. M. M., Adhikary, A and Ahmed, S., R., 2011. Nonlinear analysis of electro-thermal response of a conducting wire of dissimilar materials with variable thermal conductivity, Proc. International Conference on Mechanical Engineering 2011, Dhaka, ICME 11-AM-012, p.1-6.
[12] Saka, M. and Zhao, X., 2012. Analysis of the temperature field near a corner composed of dissimilar metals subjected to a current flow, International Journal of Heat and Mass Transfer, 55, p. 6090-6096.

Available online at www.sciencedirect.com

SciVerse ScienceDirect

Procedia Engineering 00 (2012) 000–000

Procedia
Engineering

www.elsevier.com/locate/procedia

5th BSME International Conference on Thermal Engineering

Effect of Material Property Distribution on Thermoelastic Behavior of a Rotating Circular Disk with an FGM Coating at the Outer Surface

F. A. Sohag, A. M. Afsar*

Department of Mechanical Engineering, BUET, Dhaka 1000, Bangladesh

Abstract

This study examines the thermoelastic characteristics of a thin circular disk having a concentric hole and a functionally graded material (FGM) coating at the outer surface. The disk is assumed to have power function and exponential variation of all the material properties, except the Poisson's ratio, which is assumed to be constant throughout the disk. The disk is subjected to a temperature gradient field and an inertial force due to rotation of the disk. The incompatible eigenstrain developed in the disk due to the temperature gradient field and nonuniform coefficient of thermal expansion (CTE) is taken into account. The problem is reduced to the solution of a second order differential equation which is solved by developing a finite element model based on the variational approach and Ritz method. The finite element model is demonstrated for an Al disk with an Al/Al_2O_3 FGM coating. The numerical results demonstrate that the temperature and material property distributions are the salient parameters to be considered in order to design a circular disk with an FGM coating to be used as a grinding disk or a cutter.

© 2012 The authors, Published by Elsevier Ltd. Selection and/or peer-review under responsibility of the Bangladesh Society of Mechanical Engineers

Keywords: Functionally graded materials (FGMs); Coating; Circular disk; Thermoelasticity; Thermal load; Finite element method.

Nomenclature

a	radius of hole in the disk (mm)
b	outer radius of the disk (mm)
c	coating thickness (mm)
h	thickness of homogeneous region (mm)
k	thermal conductivity (W/mK)
r	radial distance (mm)
t_a, t_b, t_h	temperature (°C)
u_r	radial displacement (mm)
A, B	constituent materials of FGM
CTE	coefficient of thermal expansion
E	Young's modulus (MPa)
FGM	functionally graded material
P	property of FGM
P_A	property of constituent material A
P_B	property of constituent material B

---

* Corresponding author. Tel.: +880-1552-415088; fax: +880-2-8613046.
E-mail address: mdafsarali@me.buet.ac.bd

T	temperature (°C)
Greek symbols	
α	coefficient of thermal expansion (/°C)
ε^*	eigenstrain (mm/mm)
ε_r, ε_θ	radial and circumferential strain components, respectively (mm/mm)
θ	angular distance (rad)
ν	Poisson' ratio
ρ	density (kg/m^3)
σ_r, σ_θ	radial and circumferential stress components, respectively (MPa)
ω	angular speed (rad/s)
Subscripts	
r	radial coordinate
θ	angular coordinate

1. Introduction

Functionally graded materials (FGMs) are a new generation of engineered materials which are a nonhomogeneous mixture of two or more distinct material phases, such as different ceramics or ceramics and metals. The key distinguishing feature of these materials is that the composition, or in other words, the material distribution of each constituent material, continuously varies with space variables. This continuously varying material distribution induces chemical, material, and microstructural gradients, and makes functionally graded materials different in behavior from homogeneous materials and traditional composite materials. FGMs have now been promising candidates for various structural components such as FGM beams [1-2] and cylinders [3-4] which are designed for diverse thermal and mechanical loading conditions.

In the studies mentioned above, attention was focused mainly on the structural performance of FGMs. To investigate the functional performance of these materials, FGM concept was explored for thermal barrier [5] and tribological [6] coatings. Furthermore, Cho and Park [7] investigated the thermoelastic characteristics of functionally graded lathe cutting tools composed of Cr–Mo steel and ceramic tip. In our previous study [8], we have demonstrated that a circular FGM cutter or grinding disk can be designed with better thermoelastic characteristics if certain parameters, namely, temperature distribution, angular speed, radial thickness, and outer surface temperature, are controlled properly. For the purpose of analyzing the thermoelastic characteristics, a finite element model was developed. However, the FGM disk considered in our previous study [8] had a material gradation throughout the entire radial thickness, i.e., from the inner surface to the outer surface of the disk. Such an FGM disk is, in fact, not practicable because of manufacturing limitations as well as cost. Furthermore, the previous study [8] was carried out for some assumed profiles of temperature distribution. In an attempt to understand the characteristics under actual conditions, the present study, therefore, focuses on the analysis of the disk only with a thin FGM coating at the outer surface, instead of an FGM disk having material gradation throughout the entire radial thickness of the disk. Further, actual temperature distributions, instead of assumed ones, are considered in the present study.

2. Modelling of FGM properties

In a circular cutter or a grinding disk, the outer surface and its adjoining region should be made of such a material that it can resist wear and high temperature while the inner region should be tougher and thermally conductive to absorb torsional energy and facilitate cooling, respectively. A simple bi-metallic disk made of ceramic at the outer surface and metal at the inner region can meet the above requirements. However, the sharp interface between ceramic and metal induces the problem of delamination and ultimate failure of the disk. To get rid of these problems, the disk can be designed with an FGM coating at the outer surface and a homogenous material at the inner portion of the disk as shown in Fig. 1. The disk has a concentric hole of radius a with an outer radius b. The region (h-a) consists of homogenous material A only. The coating region c = (b-h) consists of A/B FGM where the distribution of materials A and B varies continuously from r = h to b.

The present study adopts two categories of functions to model the variation of different properties of FGMs. The first one is the power function variation of FGM properties that can be given by

$$P = \left(P_A - P_B\right)\left(\frac{r-b}{a-b}\right)^n + P_B\ ;\ \ n \geq 0 \tag{1}$$

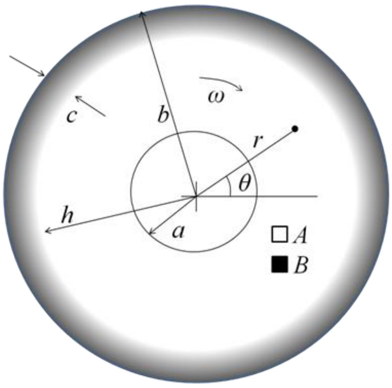

Fig.1. Schematic diagram of a disk with an FGM coating at the outer surface.

where P indicates any specific property of FGM, such as Young's modulus E, CTE α, density ρ, and the thermal conductivity k . It is noted that the Poison's ratio is assumed to be constant as its range of variation is small and has a negligible effect on the characteristics. The subscripted variables denote the respective properties of the constituent materials A and B, while the non-subscripted variables designate the properties of FGM. The exponent n is known as grading index.

The second category is the exponential variation of FGM properties and is given by

$$P = P_0 \exp(\gamma_P r) \tag{2}$$

where the constants P_0 and γ_P are determined from the boundary conditions given below.
(i) $r = a$, $P = P_A$
(ii) $r = b$, $P = P_B$.

Making use of the above boundary conditions in Eq. (2) yields

$$P_0 = P_A \exp(-\gamma_p a) \tag{3}$$

$$\gamma_p = \frac{1}{a-b} \ln\left(\frac{P_A}{P_B}\right) \tag{4}$$

Although Eqs. (1) - (4) express the properties of the FGM coating region ($h \le r \le b$), the same expressions can be utilized to determine the properties of the homogeneous region ($a \le r \le h$) by setting the values of n and γ_P to zero.

3. Formulation of the problem

The disk considered in the present study is subjected to a temperature gradient field and an inertia force due to rotation with an angular speed ω of the disk. The inner surface is assumed to be fixed to a rigid shaft while the outer surface is free from any mechanical loading. Thus, the boundary conditions can be stated as

(i) $r = a, \quad u_r = 0$; (ii) $r = b, \quad \sigma_r = 0$.

Due to nonuniform CTE and temperature gradient field, an incompatible eigenstrain is developed in the disk which is given by

$$\varepsilon^* = \alpha(r)T(r) \tag{5}$$

Here, $T(r)$ is the change in temperature at any point r of the disk. By making use of generalized heat conduction equation, temperature profile for the homogeneous portion of the disk can be derived as

$$T = t_a + \frac{(t_a - t_h)}{\ln\left[h/a\right]}\ln\left[a/r\right] \tag{6}$$

For five different profiles of k (n = 1, 3, 5, 7, 10 in Eq. (1)), the temperature distributions have been determined in the FGM region. For n = 1, it is found as

$$T = c_2 + \frac{c_1(\ln[r] - \ln[-bK_A + aK_B + K_A r - K_B r])}{(aK_B - bK_A)} \tag{7}$$

Here, the constants c_1 and c_2 are determined from the following temperature boundary conditions:

(i) $r = h, \quad T = t_h$; (ii) $r = b, \quad T = t_b$.

For other values of n (= 3, 5, 7, 10), the temperature distributions are presented graphically in Fig. 2. Again, for exponential variation of thermal conductivity as given by Eq. (2), the temperature distribution is determined as

$$T = c_2 + c_1 \mathrm{Ei}[-\lambda * r] \tag{8}$$

where Ei is the exponential integral. The constants c_1 and c_2 are determined by applying the same temperature boundary conditions mentioned earlier.

It is noted that t_a, t_b, t_h, and T represents temperature at radial distance a, b, h, and r, respectively. The temperature, t_h, at the interface ($r = h$) can be found from the fact that the heat flow out of the coating region must be the heat flow into the homogeneous region. Utilizing the thermoelastic theories and Eq. (1) for power function variation of the material properties, one can readily obtain

$$\begin{aligned} &\frac{d^2F}{dr^2} + \left[\frac{1}{r} - n\frac{E - E_B}{E(r-b)}\right]\frac{dF}{dr} + \frac{1}{r}\left[n\nu\frac{E - E_B}{E(r-b)} - \frac{1}{r}\right]F \\ &= \rho\omega^2 r\left[nr\frac{E - E_B}{E(r-b)} - nr\frac{\rho - \rho_B}{\rho(r-b)} - \nu - 3\right] - E\alpha\left[nT\frac{\alpha - \alpha_B}{\alpha(r-b)} + \frac{dT}{dr}\right] \end{aligned} \tag{9}$$

where $F = r\sigma_r$. Again, for exponential variation of the material properties as expressed by Eq. (2), the thermoelastic theories yield

$$\frac{d^2F}{dr^2} + \left(\frac{1}{r} - \beta\right)\frac{dF}{dr} + \frac{1}{r}\left(\beta\nu - \frac{1}{r}\right)F = \rho\omega^2 r\left(\beta r - \mu r - \nu - 3\right) - E\alpha\left(\gamma T + \frac{dT}{dr}\right) \tag{10}$$

Since the analytical solution of Eq. (9) is not realistic, a finite element model is developed for the numerical solution of the present problem. As all the parameters are function of r only making it a one dimensional problem, the radial domain $\Omega = (a, b)$ of the disk is divided into N number of sub domains $\Omega^e = (r_e, r_{e+1})$, where $e = 1, 2, \ldots, N$. Then following the Variational approach and Ritz method, Eq. (9) can be reduced to

$$\sum_{j=1}^{2} K_{ij}^e F_j^e = L_j^e \tag{11}$$

where

$$K_{ij}^e = B(\phi_i^e, \phi_j^e) \tag*{12(a)}$$

$$L_i^e = l(\phi_i^e) \tag*{12(b)}$$

$$F = \sum_{j=1}^{2} F_j^e \phi_j^e \tag*{12(c)}$$

$$B(w,F) = \int_{r_e}^{r_{e+1}} \frac{dw}{dr}\frac{dF}{dr}dr - \int_{r_e}^{r_{e+1}} \left[\frac{1}{r} - n\frac{E-E_B}{E(r-b)}\right] w\frac{dF}{dr}dr - \int_{r_e}^{r_{e+1}} \frac{1}{r}\left[n\nu\frac{E-E_B}{E(r-b)} - \frac{1}{r}\right] wFdr \tag*{12(d)}$$

$$l(w) = -\int_{r_e}^{r_{e+1}} wf(r)\,dr + w(r_{e+1})\frac{dF}{dr}(r_{e+1}) - w(r_e)\frac{dF}{dr}(r_e) \tag*{12(e)}$$

Following exactly the same approach, the second governing differential equation (Eq. (10)) can be discretized similarly as Eq. (11). Equation (11) is a system of algebraic equation, which can be used to form a global system of algebraic equation by satisfying the continuity condition $F_2^e = F_1^{e+1}$. Once the values of *F* are known at the global node points, the components of stress, strain, and displacement are obtained from:

$$\sigma_r = \frac{1}{r}\sum_{j=1}^{2} F_j^e \phi_j^e \tag*{12(a)}$$

$$\sigma_\theta = \sum_{j=1}^{2} F_j^e \frac{d\phi_j^e}{dr} + \rho\omega^2 r^2 \tag*{(12(b)}$$

$$\varepsilon_r = \frac{1}{E}\sum_{j=1}^{2}\left[\frac{F_j^e \phi_j^e}{r} - \nu F_j^e \frac{d\phi_j^e}{dr}\right] - \frac{\nu\rho\omega^2 r^2}{E} + \varepsilon^* \tag*{(13(a)}$$

$$\varepsilon_\theta = \frac{1}{E}\sum_{j=1}^{2}\left[F_j^e \frac{d\phi_j^e}{dr} - \frac{\nu}{r} F_j^e \phi_j^e\right] + \frac{\nu\rho\omega^2 r^2}{E} + \varepsilon^* \tag*{13(b)}$$

$$u_r = \frac{r}{E}\sum_{j=1}^{2}\left[F_j^e \frac{d\phi_j^e}{dr} - \frac{\nu}{r} F_j^e \phi_j^e\right] + \frac{\nu\rho\omega^2 r^3}{E} + \varepsilon^* r \tag*{(14)}$$

4. Numerical results and discussion

The finite element model developed in the study is demonstrated for an Al disk with an Al_2O_3 /Al FGM coating at the outer surface. In fact, the symbols *A* and *B* used in the theoretical models can be any materials depending on design requirements. However, in the present study, Al and Al_2O_3 have been chosen for *A* and *B*, respectively, as an example. The required properties such as Young's modulus, CTE, density, and thermal conductivity of Al are taken as 71 MPa, 23.1×10^{-6} / ^{0}C, 2700 kg/m^3, and 204 W/mK, respectively. The corresponding properties of Al_2O_3 are 380 MPa, 8.0×10^{-6}/ ^{0}C, 960 kg/m^3, and 35 W/mK, respectively. The Poisson's ratio is taken as 0.3, which is kept constant throughout the disk.

From convergence test, it is found that the element size of 1 mm ensures the convergence of the results. Therefore, all the numerical results present in this section correspond to element size of 1 mm.

To examine the effect of material property distribution on the thermoelastic characteristics, six different profiles given by Eq. (1) (n = 1, 3, 5, 7, 10) and Eq. (2) are considered. For these prescribed profiles, temperature distributions calculated are shown in Fig. 2. Using the material properties of Eqs. (1) and (2) and the corresponding actual temperature distribution of Fig. 2, displacement and stress components are computed, which are depicted in Figs. 3 to 5. All the results correspond to t_a = 20 °C and t_b = 150 °C. As seen from Fig. 3, for all the material property distributions, the displacement is the minimum at the inner surface and it monotonically increases toward the outer surface of the disk except at the interface between the

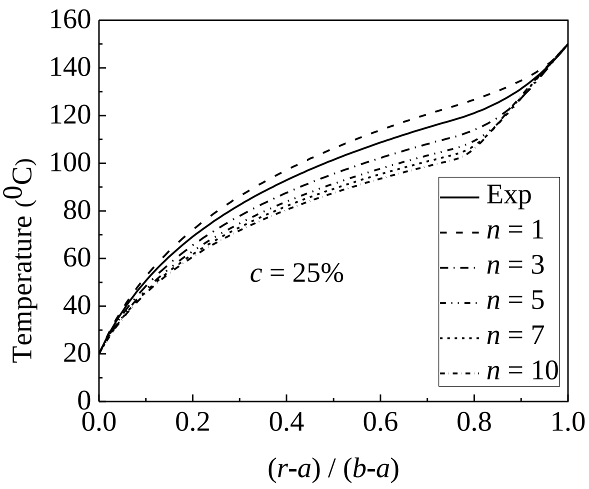

Fig. 2. Temperature distribution profile.

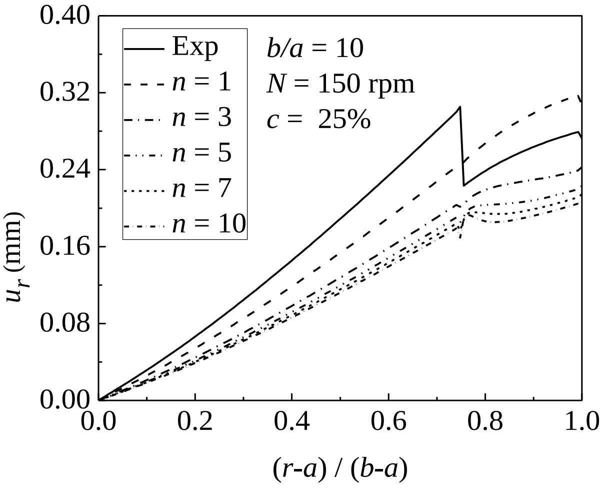

Fig. 3. Effect of material distribution on radial displacement.

homogeneous region and FGM coating for the exponential profile, where the magnitude of the displacement suddenly falls and then increases continuously towards the outer surface. Apart from the outer FGM coating region, radial displacement is the maximum for the exponential profile over the homogeneous portion and minimum for *n* = 1 as shown in Fig 3. For any material distribution, the radial displacement is zero at the inner surface, which satisfies the boundary condition of the problem.

Figure 4 shows the effect of material property distribution on radial stress. For all the six material property distributions, radial stress is tensile over the inner region of the disk and compressive over the outer region of the disk. This type of stress distribution is in fact desirable as the outer region of the disk is ceramic (Al_2O_3) rich, which has better compressive strength. On the other hand, the inner region consists of purely metallic material (Al), which has better tensile strength. Further, it is noted that the exponential material property distribution develops the maximum tensile stress at the inner region. As seen from Fig. 5, over the major portion of the homogeneous region of the disk, circumferential stress is compressive which is the maximum for *n* = 10. Over approximately 10% of the outer region of FGM coating, the stress is tensile which is the maximum for *n* = 1.

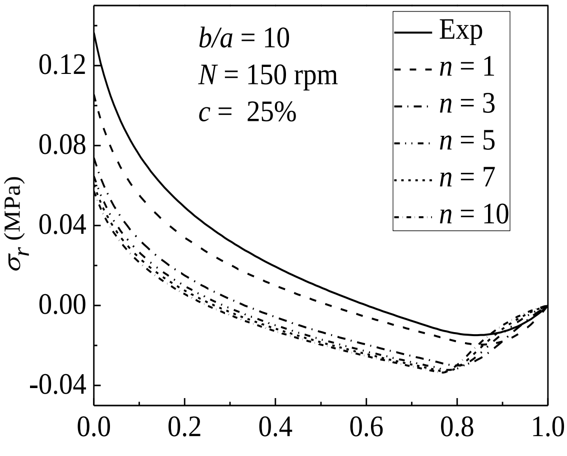

Fig. 4. Effect of material distribution on radial stress.

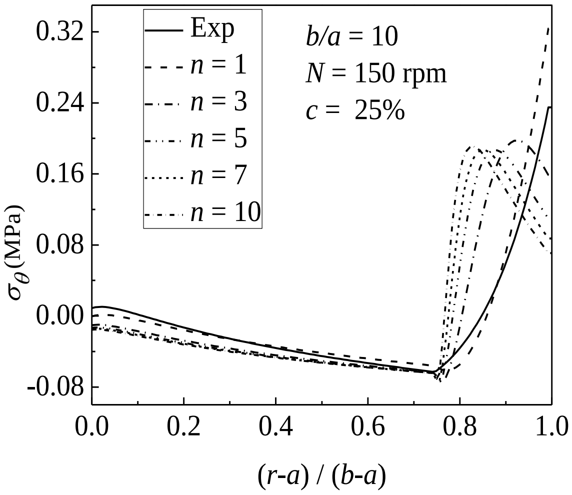

Fig. 5. Effect of material distribution on circumferential stress.

5. Conclusion

A finite element model has been developed for a rotating circular disk with an FGM coating at the outer surface for the analysis of thermoelastic characteristics of the disk. The model can also be applied to an FGM disk with a material gradation throughout the entire radial thickness by setting $h = a$ and to a homogeneous disk by setting the parameters n and γ_P to zero. Thus, the present model is more comprehensive and can be used to design a circular cutter or a grinding disk ensuring better thermoelastic characteristics in an actual application. The numerical results presented in the study indicate that the material distribution in the FGM coating region plays an important role to characterize thermoelastic behaviors and hence selection of proper material distribution is an important issue that should be determined by a suitable optimization technique.

Acknowledgement

The authors would like to acknowledge the partial support of the Committee for Advanced Studies and Research (CASR) of Bangladesh University of Engineering and Technology (BUET).

References

[1] Xiang, H. J., Yang, J., 2008. Free and Forced Vibration of a Laminated FGM Timoshenko Beam of Variable Thickness under heat Conduction, Composites Part B 39, p. 292.

[2] Li, S. R., Zhang, J. H., Zhao, Y.-G., 2006. Thermal Post-Buckling of Functionally Graded Material Timoshenko Beams, Applied Mathematics and Mechanics 27, p. 803.

[3] Obata, Y., Noda, N., 1994. Steady Thermal Stresses in a Hollow Circular Cylinder and a Hollow Sphere of a Functionally Graded Material, Journal of Thermal Stresses 17, p. 471.

[4] Liew, K. M., Kitipornchai, S., Zhang, X. Z., Lim, C. W., 2003. Analysis of the Thermal Stress Behavior of Functionally Graded Hollow Circular Cylinders, International Journal of Solids and Structures 40, p. 2355.

[5] Xiao, J. S., Jiang, B., Liu, J., Huang, S. Y., 2003. Microstructures and Mechanical Properties of Ceramic/Metal Gradient Thermal Barrier Coatings, Journal of Wuhan University of Technology 18, p. 1000.

[6] Prchlik, L., Vaidya, A., Sampath, S., 2000. “Damage Tolerant Tribological Coatings Based on Thermal Sprayed FGMs,” 6th International Symposium on Functionally Graded Materials. Estes Park, Colorado, USA, 10–14.

[7] Cho, J. R., Park, H. J., 2002. High Strength FGM Cutting Tools: Finite Element Analysis on Thermoelastic Characteristics, Journal of Materials Processing Technology 130 – 131, p. 351.

[8] Go, J., Afsar, A. M., Song, J. I., 2010. Analysis of Thermoelastic Characteristics of a Rotating FGM Circular Disk by Finite Element Method, Advanced Composite Materials 19, p. 197.

Available online at www.sciencedirect.com

SciVerse ScienceDirect

Procedia Engineering 00 (2012) 000–000

Procedia Engineering

www.elsevier.com/locate/procedia

5th BSME International Conference on Thermal Engineering

Effect of Carbon Nanofibers on Thermal Conductivity of Carbon Fiber Reinforced Composites

Junfeng Liang, Mrinal C. Saha*, M. Cengiz Altan

School of Aerospace and Mechanical Engineering, University of Oklahoma, Norman, OK 73019, USA

Abstract

Carbon fiber-reinforced composites (CFRCs) have been fabricated using a vacuum assisted resin transfer molding (VARTM) incorporating carbon nanofibers (CNFs). Incorporation of CNFs in the composite laminate was performed by both matrix-modification and fiber-modification routes. In the matrix-modification route, vapor grown carbon nanofibers (VGCNFs) were directly mixed into the epoxy resin EPON862 using ultrasound tip sonication. In the fiber-modification route, carbon nanofibers (CNFs) were directly grown on the carbon fiber fabric using chemical vapour deposition (CVD). A wire-based 3ω technique was used to measure the thermal conductivity of the CFRCs in both in-plane and through-thickness direction. Although the matrix-modification route didn't show significant improvement in the in-plane direction, the fiber-modification route showed improvement in both in-plane and through-thickness directions. Maximum improvement in through-thickness thermal conductivity of about 10% and 30% was observed in the matrix-modification and fiber-modification route, respectively. It is believed that the random orientation of the CNFs on the fiber surface results in such an improvement in the in-plane direction. Effect of temperature on thermal conductivity was also measured and found to be significant for the CNF-modified composites compared to unmodified composites.

© 2012 The authors, Published by Elsevier Ltd. Selection and/or peer-review under responsibility of the Bangladesh Society of Mechanical Engineers

Keywords: Carbon nanofiber, Carbon fiber reinforced composites, Thermal conductivity

---

1. Introduction

Carbon fiber reinforced composites (CFRCs) are currently being used in a variety of applications ranging from sporting goods to space craft due to their superior specific properties. Recently, there has been increased interest in using CFRCs in thermal management applications such as integrated circuits, rocket motors and SLASR technology [1, 2]. Extensive research and development in CFRCs led to remarkable improvements in the in-plane thermal properties; however, these composites typically show poor through-thickness thermal conductivity where heat conduction is dominated by the polymer matrix. The low thermal conductivity of the polymer matrix serves as an insulation layer for heat transfer between layers in CFRCs which results in three to seven folds difference in thermal conductivity between the in-plane and through-thickness directions [3, 4]. Through-thickness thermal conductivity can be improved by incorporating conductive pathways between the layers of CFRCs.

---

* Corresponding author. Tel.: +1-405-325-1098; fax: +1-405-325-1088.
E-mail address: msaha@ou.edu

Carbon nanotubes (CNTs) have been suggested as an ideal candidate as a conductive filler for polymer matrix and inter-ply matrix-rich regions in CFRCs due their nanoscale dimensions and outstanding thermal properties (about 3000 W/mK) [5]. Vapor grown carbon nanofibers (CNFs) also reported to have superior thermal conductivity (about 1900 W/mK) [6] and there are already some studies reporting improvement in thermal conductivity of CFRCs using CNFs via matrix-modification route [7, 8]. One major issue with the matrix-modification route is the increase in viscosity with the increase in nanofiller content which results in non-uniform dispersion and improper impregnation of fibers with matrix during composite processing [9]. Another issue with this approach is the possibility of filtration of nanofillers by the microfiber bed during the impregnation process [10-13]. Moreover, interfacial thermal resistance between the nanofiller and matrix is very high which results in poor through-thickness thermal conductivity of the CFRCs.

A number of studies have reported modification of fiber surface either by spraying or direct growing conductive fillers such as CNTs and CNFs to enhance CFRCs properties including thermal conductivity [14-22]. Downs and Baker [14, 15] pioneered in growing nanofibers on micro-fibers to form hierarchical structures using chemical vapor deposition (CVD). Thostenson et al. [16] successfully synthesised CNTs via CVD on the surface of carbon fibers using pre-deposited metal catalyst. Recently, Bipul et al. [22] investigated spray deposited CNTs on mechanical performance of CFRCs and reported about 25% improvements in flexure properties with 0.3% CNTs. While most of the work focused on mechanical properties of CFRCs with CNTs or CNFs, a very few research reported on thermal conductivity of CFRCs with grafted CNTs or CNFs. Veedu et al. [23] was probably the first group to report about 50% improvement in through-thickness thermal conductivity of SiC composites containing grafted CNTs.

In this paper, we report on thermal conductivity of CFRCs containing CNFs for both resin-modification and fiber-modification routes. Effect of CNFs and temperature on both in-plane and through-thickness thermal conductivities of these two types of CFRCs were reported.

2. Experimental

2.1. Materials

The resin used in this study is EPON862 with EPIKURE curing agent W system. The viscosity of the uncured resin is about 2200 cp at room temperature and about 30 cp at 120°C. The dry fabric used in this research was T-650/35 PAN-based plain weave carbon fiber. The density of the carbon fabrics is 1.77 g/cc and the thermal conductivity of carbon fabric based on tow is about 14 W/mK. Vapor grown carbon nanofibers (CNFs) used in this study was Pyrograf III PR24 with diameter: 60-150 nm; length: 30-100 μm; thermal conductivity: 1950 W/mK. The nanofibers were obtained from Applied Sciences and used for fabricating the nanofiber-filled CFRCs.

2.2. CNF Growth on Carbon Fabric

Chemical vapor deposition (CVD) was used to grow CNFs on carbon fabric. Various amounts of nickel nitrate and copper nitrate salts were mixed in isopropanol and deposited on the surface of the carbon fabric by spraying the solution directly onto the fabrics. The carbon fabric was then inserted into a quartz reaction tube in a three zone vertical furnace (Fig.1). The catalyst was calcined in air at 300°C for 1 hour to convert from metal nitrates to oxides, and then reduced in pure hydrogen at 500°C for 30 minutes to de-oxidize the catalyst nanoparticles. Ethylene was introduced into the reaction tube to serve as a carbon source for the CNF growth, which took place at 700°C for 30 minutes. The reaction tube was then purged and the samples were cooled to room temperature in a pure nitrogen environment. Mass of the fabric was measured before and after reaction to determine the percentage of growth of CNFs. Table 1 shows different amount of carbon fiber containing CNFs in the CFRCs. Scanning electron microscope (SEM) and transmission electron microscope (TEM) were also used to investigate the CNFs structure and the morphology of the growth (Fig.2).

CFRCs with two different amount of CNFs growth were studied in work. The amount of CNFs was controlled by the weight percentage of the catalyst sprayed on the carbon fabric. The detail of the growth was shown in Table 1.

Table 1 Amount of CNFs growth on carbon fiber fabric

Sample ID	wt % of catalyst	wt % of CNFs
CFF9	3	240
CFF10	1.2	82
110210-1-8	0.2	8.193
101410-1-8	0.3	17.473
102010-1-8	0.2	5.146

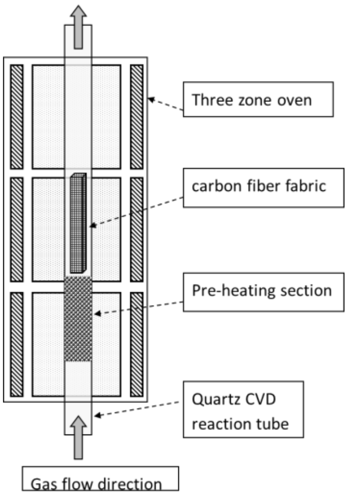

Fig. 1 Schematic for chemical vapor deposition (CVD) process for CNF growth on carbon fabric.

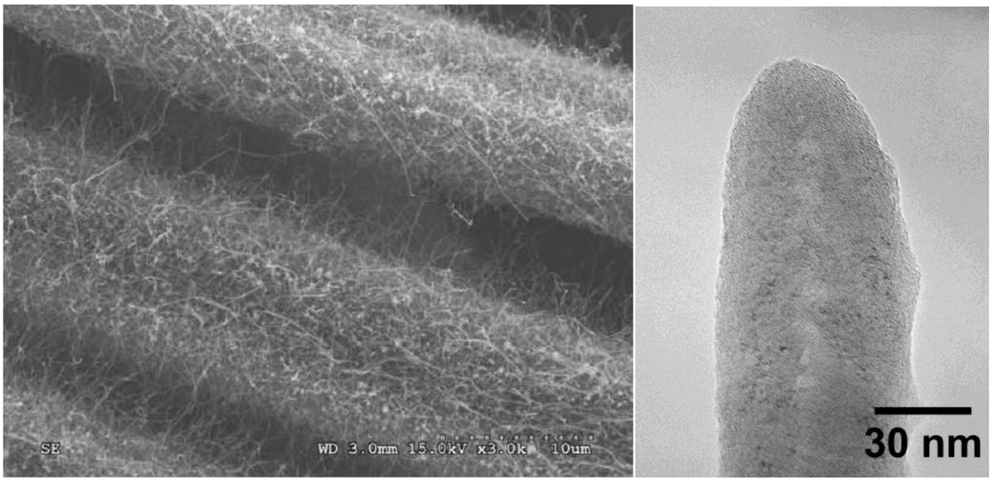

(a) (b)

Fig. 2. (a) SEM images carbon fiber fabric with CNF growth during CVD (b) TEM image of the CNF growth on carbon fabric.

2.3. Carbon Composites Preparation

The CFRCs were manufactured using a vacuum assisted resin transfer molding (VARTM) process incorporating a reference dam. Several layers of fabrics (with and without CNF growth) are laid up on an aluminium tool plate. The fabrics are aligned with a reference dam to create a straight edge after curing of the composite laminate. Vacuum pressure was used to impregnate dry preform with the matrix drawn into and through the layup following the path depicted in Fig. 3. The resin was heated up to approximately 121°C before infusion and was maintained at this temperature until the infusion was finished. After infusion, the sample was heated up to 177°C and maintained at this temperature for 90 minutes, and then allowed to be naturally cooled overnight. The integrity of the vacuum bag is verified by checking that the leak rate was less than 25 mm of mercury in five minutes.

For modification of matrix route, CNFs were first mixed with resin and tip sonicated for 30 minutes at 40% power amplitude using a VCX 750 W/cm^2, and then mechanically mixed for 10min at 250rpm with cure agent. This mixture was then used with the abovementioned molding process. In this study, the weight fraction of CNF was chosen as 0.1%.

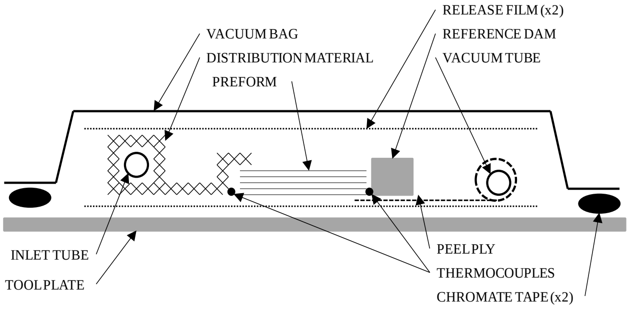

Fig. 3 Schematic of the cross section of VARTM layup. The resin will flow from the inlet tube on the left, through the preform to the vacuum tube on the right.

2.4. Sample Preparation for Thermal Conductivity

The manufactured CFRC panel was polished on the surface using a glass grinder (Glassworks JackR) with sanding pads of different grits sequentially (400, 800, 1200, 2000). Polishing time for each pad of different grit was about 30 minutes to ensure the final surface condition of the CFRC panel was flat and smooth. The CFRC panel was then cut into small testing specimen about 1cm long and 0.25 wide. Spin-on-glass (Futurrex IC1-200) was used to be coated on the specimen surface to insulate the exposed fabric after polishing.

2.5. Measurement of Thermal Conductivity

A hot wire 3ω method was used to measure the thermal conductivity of composite samples at different temperature. In this method, a 10μm diameter platinum wire was mounted on the polished surface of a small CFRCs sample. Spin-on-glass was used as adhesive to ensure a good contact between the sample and the wire. The wire served as both heating and sensing element for the test. The sample was connected to the experimental setup with lead wires. A sinusoidal voltage at frequency ω was applied to the sample surface through the wire element shown in Fig.4. The surface temperature thus oscillated at a frequency of 2ω. This oscillation caused the wire resistance to fluctuate and combining with the primary driving current generate a secondary signal of a frequency of 3ω which was captured by the lock-in amplifier in the setup. By fitting this signal to the analytical model, thermal conductivity of the sample can be back calculated. [24, 25]. Additionally, the temperature of the measurement environment was controlled with a cryostat chamber, thus thermal conductivity of different temperature could be also measured.

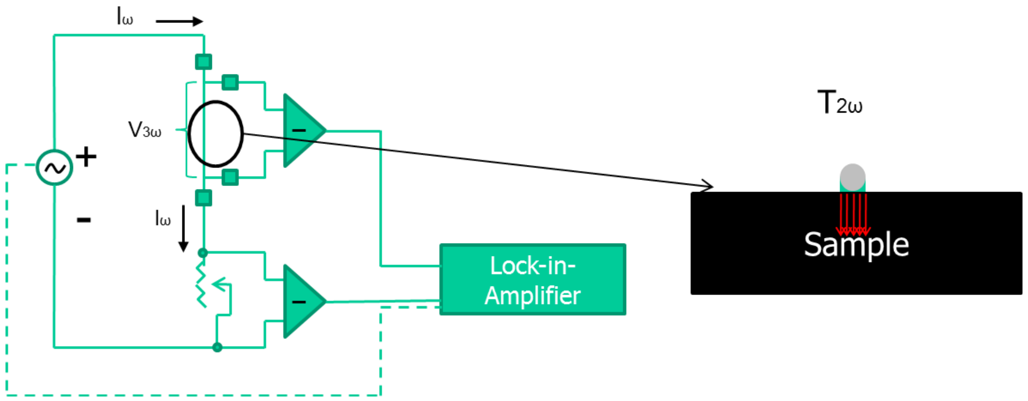

Fig. 4 Schematic of 3ω thermal conductivity measurement setup (left) and the sample with platinum wire mount (right).

3. Results and Discussion

Figure 5(a) shows the planar thermal conductivity of the CNF filled CFRCs. There is no significance enhancement of thermal conductivity compared to the neat composite laminate in the in plane direction. The reason for this is that the thermal conductivity of epoxy-CNF system is much lower than the longitude thermal conductivity of the carbon fabric [26]. In longitude direction, the thermal conductivity of the composites is still dominated by the carbon fabric system. Fig. 6(b) shows the through-thickness thermal conductivity of the CNF filled CFRCs. There is about 10% enhancement of thermal conductivity in this direction. This stems from the improvement of thermal conduction in the resin-rich area between the laminate layers. Nevertheless, due to the limited amount of CNF distributed, the enhancement of through-thickness direction is not substantial.

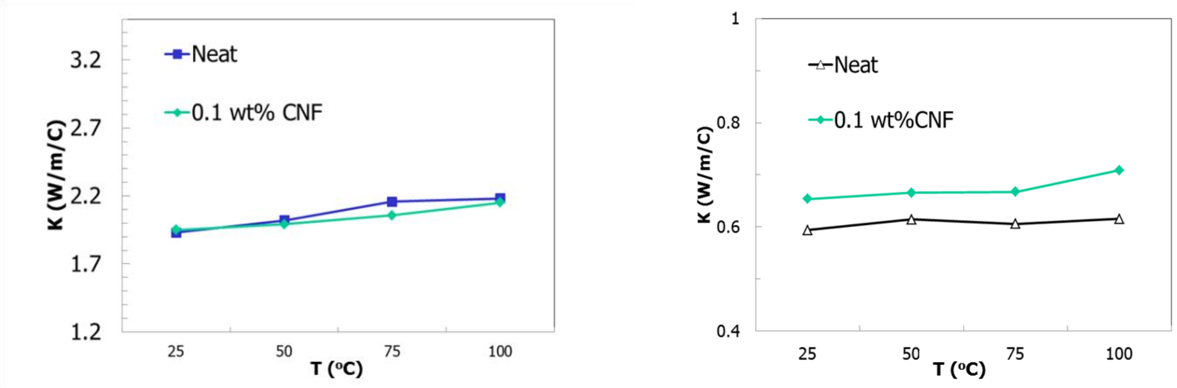

(a) (b)

Fig. 5(a) In-plane thermal conductivity of CNF filled CFRCs at various temperatures. (b) Through-thickness thermal conductivity of CNF filled CFRCs at various temperatures

Fig. 6(a) shows the planar thermal conductivity of the CNF grown CFRCs. With low amount of growth, again there is no significant change of the thermal conductivity of the composites. But when growth increases to 250 wt% there is about 10% enhancement, and the enhancement increases as temperature increases. The reason for this could be due to the bending of the CNF forest by the vacuum pressure, thus aligning them in-plane direction. Enhancement of thermal conductivity in the through-thickness direction is much more significant. The largest enhancement is obtained with 252 wt% growth where about 33% improvement is shown in Fig. 6(b). With higher growth of CNFs, more CNFs were bridging between the reinforcement and the matrix and thus overcoming the effect of phonon scattering.

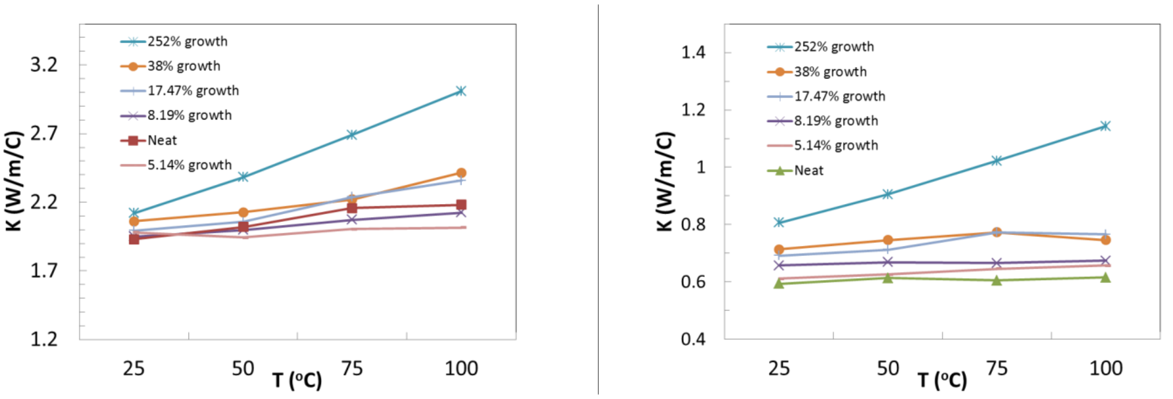

(a) (b)

Fig. 6(a) In-plane thermal conductivity of CNF grown CFRCs at various temperatures. (b) Through-thickness thermal conductivity of CNF grown CFRCs at various temperatures

It is mentioned that the volume fractions of fiber in the composites with CNFs growth are in the range from 42-48 wt% whereas the volume fraction of fiber in the neat composite is about 60 wt%. According to the finite element analysis reported in the literature [27] the through-thickness thermal conductivity depends on the volume fraction of fiber in the composite. Since CRFCs with CNFs growth has smaller fiber content the through-thickness thermal conductivity values are corrected for the same fiber content as neat CFRCs (e.g. 60 wt%) using the empirical relationship of the data [27] shown in Fig. 7(a). Fig. 7(b) shows the corrected through-thickness thermal conductivity of CFRCs with CNF growth normalized with the neat CFRCs containing the same carbon content at room temperature. It can be seen that the through-thickness thermal conductivity of CFRCs with 252 wt% CNFs growth is about 9 times higher than the neat CFRCs. Even with modest CNFs growth in the amount of 5 wt% the increase in through-thickness thermal conductivity is about 60%, which is significantly higher than CNF filled CFRCs. Therefore, modification carbon fabric with CNFs growth is more effective to enhance through-thickness thermal conductivity of CFRCs. Considering that CNFs is generally lighter than carbon fiber, introducing CNFs into CFRCs opens new ways to fabricate light weight structure with improved through-thickness thermal conductivity.

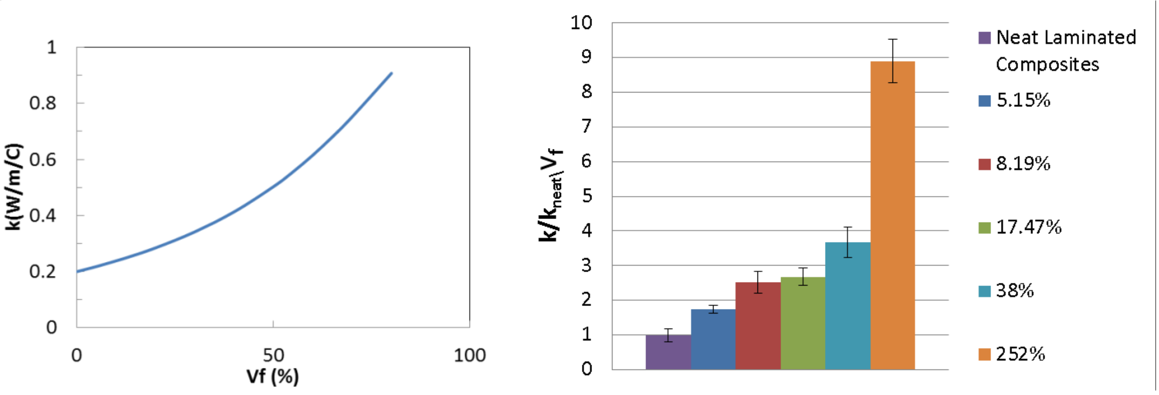

(a) (b)

Fig. 7 (a). Predicted through-thickness thermal conductivity of CFRCs as a function of volume fraction of carbon fiber [27].(b)Normalized through-thickness thermal conductivity of CFRCs with CNFs growth containing 60% fiber content at room temperature. The vertical axis represents thermal conductivity normalized by the thermal conductivity of neat composites. The percentages indicate the growth in weight percent.

4. Conclusions

Effect of CNFs on thermal conductivity of CFRCs fabricated using VARTM was investigated. Incorporation of CNFs in the composite laminate was performed using both matrix-modification and fiber-modification routes. In the matrix-modification route, vapor grown carbon nanofibers (CNFs) were directly mixed into the epoxy resin EPON862 using ultrasound tip sonication. In the fiber-modification route, carbon nanofibers (CNFs) were directly grown on the carbon fiber fabric using a chemical vapor deposition (CVD). A wire-based 3ω technique was used to measure the thermal conductivity of the CFRCs. Although the matrix-modification route didn't show significant improvement in the in-plane direction, the fiber-modification route shows considerable improvement in both in-plane and through-thickness directions. It is believed that the random orientation of the CNFs on the fiber surface results in such an improvement in the in-plane direction. Although maximum through-thickness thermal conductivity improvement for the CFRCs with CNF growth is found to be 33%, considering the same fiber content this improvement is predicted to be as high as 9 times compared to the neat composite.

Acknowledgements

The authors acknowledge AFOSR funding of this work through the grant number FA 9550-10-1-0031. We also acknowledge Cytec Engineered Materials for providing the T650/35 dry carbon fiber fabric that used in this study.

References

[1]. Park, J. K, Cho, D., and Kang, T. J., 2004. A comparison of the interfacial, thermal, and ablative properties between spun and filament yarn type carbon fabric/phenolic composites, Carbon 42, p. 795.
[2]. Silva, C., Marotta, E., and Schuller, M., 2007. In-plane thermal conductivity in thin carbon fiber composites, Journal of Thermophysics and Heat Transfer 21, p. 460.
[3]. Biercuk, M. J., Llaguno, M. C., Radosavljevic, M., Hyun, J. K., Johnson, A. T., and Fischer, J. E., 2002. Carbon nanotube composites for thermal management, Applied Physics Letter 80, p. 2767.
[4]. Hind, S., and Robitaille, F., 2010. Measurement, Modeling, and Variability of Thermal Conductivity for Structural Polymer Composites. Polymer Composites 31, p. 847.
[5]. Berber, S., Kwon, Y. K., and Tomanek, D., 2000. Unusually high thermal conductivity of carbon nanotubes, Physical Review Letters 84, p. 4613.
[6]. Kim, P., Shi, L., Majumdar, A., and McEuen, P. L., 2001. Thermal transport measurements of individual multiwalled nanotubes. Physical Review Letters 87.
[7]. Assael, M. J., Antoniadis, K. D., and Metaxa, I. N., 2009. Measurements on the enhancement of the thermal conductivity of an epoxy resin when reinforced with glass fiber and carbon nanotubes, Journal of Chemical & Engineering Data 54, p. 2365.
[8]. Kim, Y. A., Kamio, S., Tajiri, T., Hayashi, T., Song, S. M., and Endo, M., 2007. Enhanced thermal conductivity of carbon fiber/phenolic resin composites by the introduction of carbon nanotubes. Applied Physics Letters 90.
[9]. Gojny, F. H., Wichmann, M. H. G., Fiedler, B., and Schulte, K., 2005. Influence of different carbon nanotubes on the mechanical properties of epoxy matrix composites, Composites Science and Technology 65, p. 2300.
[10]. Sadeghian, R., Gangireddy, S., Minaie, B., and Hsiao, K., 2006. Manufacturing carbon nanofibers toughened plyester/glass fiber composites using vacuum assisted resin transfer molding for enhancing the mode-I delamination resistance, Compostes Part A. 37, p. 1787.
[11]. Aktas, L., Bauman, D. P., Bowen, S. T., Saha, M. C., and Altan, M. C., 2011. Effect of distribution media length and multiwalled carbon nanotubes on the formantion of voids in VARTM composites, Journal of Engineering Materials and Technology, 133, #: 041006.
[12]. Aktas, L., Dharmavaram, S., Hamidi, Y. K., and Altan, M. C., 2008. Filtration and breakdown of clay clusters during resin transfer molding of nanoclay/glass/epoxy composites, Journal of Composite Materials 42, p. 2209.
[13]. Aktas, L., Hamidi, Y. K., and Altan, M. C., 2008. Dispersion charactrerization of nanoclay in molded epoxy disks by combined image analysis and wavelength dispersive spectrometry, Journal of Engineering Materials and Technology, 130, #: 031005.
[14]. Downs, W. B., and Baker, R. T. K., 1991. Novel Carbon Fiber-Carbon Filament Structures, Carbon 65, p. 2300.
[15]. Downs, W. B., Baker, R. T. K., 1995. Modification of the suface properties of carbon fibers via the catalytic growth of carbon nanofibers, Journal of Materials Research 10, p. 625.
[16]. Thostenson, E. T., Li, W. Z., Wang, D. Z., Ren, Z. F., and Chou, T. W., 2002. Carbon nanotube/carbon fiber hybrid multiscale composites. 91, p. 6034.
[17]. Mathur, R. B., Chatterjee, S., and Singh, B. P., 2008, Growth of carbon nanotubes on carbon fibre substrates to produce hybrid/phenolic composites with improved mechanical properties, Composites Science and Technology 68, P. 1608.
[18]. Garcia, J. E., Wardel, B. L., Hart, A. J., and Yamamoto, N., 2008. Fabrication and multifunctional properties of a hybrid laminate with aligned carbon nanotubes grown in situ, Composites Science and Technology 68, p. 2034.
[19]. Wicks, S. S., de Villoria, R. G., and Wardle, B. L., 2010. Interlaminar and intralaminar reinforcement of composite laminates with aligned carbon nanotubes, Composites Science and Technology 70, P. 20.
[20]. Bekyarova, E., Thostenson, E.T., Yu, A. Kim, H., Gao, J., Tang, J., Hahn, H. T., Chou, T. W., Itkis, M. E., and Haddon, R. C., 2007. Multiscale carbon nanotube-carbon fiber reinforcement for advanced epoxy compostes, Langmuir 23, p. 3970.
[21]. Zhang, Q. H., Liu, J. W., Sager, R., Dai, L. M., and Baur, J., 2009. Hierarchical composites of carbon nanotubes on carbon fiber: influence of growth condition on fiber tensile properties, Composites Science and Technology 69, p. 594.
[22]. Barua, B., Saha, M.C., 2012. Ultrasound assisted hybrid carbon epoxy composites containing carbon nanotubes, Journal of Engineering Materials and Technology, under review
[23]. Veddu, V. P., Cao, A. Y., Li, X. S., Ma, K. G., Soldano, C., Kar, S., Ajayan, P. M., and Ghasemi-Nejhad, M. N., 2006. Multifunctional composites using reinforced laminate with carbon-nanotube forests, Nature Materials 5, p. 457.
[24]. Cahill, D. G., 1990. Thermal-Conductivity Measurement from 30-K to 750-K - the 3-Omega Method, Review of Scientific Instruments 61, p. 802.
[25]. Olson, B. W., Graham, S., and Chen, K., 2005. A practical extension of the 3 omega method to multilayer structures, Review of Scientific Instruments 76.

[26]. Karippal, J. J., Murthy, H. N. N., Rai, K. S., Krishna, M., and Sreejith, M., 2010, Effect of amine functionalization of CNF on electrical, thermal, and mechanical properties of epoxy/CNF composites, Polymer Bull 65, p. 849.
[27]. Kulkarni, M. R., and Brady, R. P., 1997. A model of global thermal conductivity in laminated carbon/carbon composites, Composites Science and Technology 57, p. 277.